Journal of Materials Chemistry A

ROYAL SOCIETY OF CHEMISTRY

REVIEW

View Article Online
View Journal

Cite this: DOI: 10.1039/c9ta11245f

Received 12th October 2019
Accepted 9th December 2019

DOI: 10.1039/c9ta11245f

rsc.li/materials-a

Nucleation and crystal growth control for scalable solution-processed organic–inorganic hybrid perovskite solar cells

Hanlin Hu,[ab] Mriganka Singh,[cd] Xuejuan Wan,*[a] Jiaoning Tang,[a] Chih-Wei Chu[d] and Gang Li*[bc]

Over the past decade, intensive research efforts have been directed toward the field of organic–inorganic hybrid perovskites, with dramatic progress made in both the photovoltaic performance and device stability. Therefore, it has become the fastest growing photovoltaic research area. Perovskite materials use low-cost earth-abundant elements and can be solution-processed; furthermore, the technology is compatible with large-scale roll-to-roll manufacturing. Recently, the successful demonstration of the photovoltaic performance of perovskites reaching that of the commercialized monosilicon photovoltaic technology combined with the significantly improved stability has made scaling-up the perovskite PV technology to become a new research area, which is the topic of this review. First, the fundamental background knowledge of classical nucleation and crystal growth from a solution is summarized along with its application in perovskite film evolution. We then discuss the common perovskite PV device architectures and perovskite layer deposition methods, followed by summarizing scalable solution approaches with recent progress and related challenges for the scaling-up process. Upon the introduction of the current in-depth understanding of perovskite nucleation and crystal growth, external strategies (including both physical and chemical approaches) controlling the perovskite film formation are reviewed in diverse scalable manufacturing methods. Overall, aiming at overcoming the challenges of transferring from

[a]Shenzhen Key Laboratory of Polymer Science and Technology, College of Materials Science and Engineering, Shenzhen University, Shenzhen 518060, China. E-mail: wanxj@szu.edu.cn

[b]The Hong Kong Polytechnic University Shenzhen Research Institute, Shenzhen 518057, Guangdong, China

[c]Department of Electronic and Information Engineering, The Hong Kong Polytechnic University, Hong Hum, Hong Kong 999077, China. E-mail: gang.w.li@polyu.edu.hk

[d]Research Center for Applied Sciences, Academia Sinica, Taipei 115029, Taiwan

Hanlin Hu received his PhD degree from the Department of Materials Science and Engineering at the King Abdullah University of Science and Technology (KAUST), Jeddah, Kingdom of Saudi Arabia, in October 2017. Then, he worked as a postdoctoral fellow in Prof. Gang Li's group in the Department of Electronic and Information Engineering, Hong Kong Polytechnic University, Hong Kong. He became an Associate Researcher in the College of Materials Science and Engineering at Shenzhen University in March 2019. His research interests include synchrotron-based crystallography characterization, printing thin-film solar cells, and transistors.

Mriganka Singh has been a combined PhD student in Prof. Hong-Cheu Lin's group in the Department of Materials Science and Engineering, NCTU, and Prof. Chih-Wei Chu's group in the Research Center for Applied Sciences, Academia Sinica, since 2015. She was a visiting PhD student in Prof. Gang Li's group in the Department of Electronic and Information Engineering, Hong Kong Polytechnic University (2017–2018). She obtained her BS (Physics) degree from Allahabad University in 2012 and MS (Physics) degree from the Indian Institute of Technology, Guwahati, in 2014. Her research focuses on the development of novel metal oxide transporting layers for hybrid perovskite solar cell applications.

laboratory research, we provide an overview of achieving high-performance perovskite solar cells by using scalable fabrication methods *via* precise nucleation and crystal growth control during the perovskite film formation process.

1. Introduction

Organic–inorganic hybrid perovskites have emerged as a unique member of third-generation solar cells with certified power conversion efficiency (PCE) exceeding 25% for single-junction devices,[1] indicating a genuinely bright future for their photovoltaic (PV) applications. There are several intrinsic material properties that contribute toward the demonstrated high PCE of perovskite solar cells (PSCs), including high absorption coefficients,[2–6] flexible bandgap tuning,[7–9] high defect tolerance,[10–12] high mobility, and long carrier diffusion length.[13–15] In addition to the excellent photovoltaic performance, low-temperature and solution-processed light-harvesting materials can facilitate the low-cost fabrication of photovoltaic devices at the industrial scale, revealing significant advantages as compared to the existing commercialized photovoltaic technologies.[16–18] Typically, perovskites exhibit a 3D crystal structure composed of three types of primary ions with the formula ABX_3, where A is a monovalent cation (such as formamidinium (FA^+), methylammonium (MA^+), or cesium (Cs^+)), B is a divalent metallic cation (such as Pb^{2+} or Sn^{2+}), and X is a halide (I^-, Br^-, or Cl^-). In 2009, initial studies involving organometal trihalides ($CH_3NH_3PbBr_3$ and $CH_3NH_3PbI_3$) used as sensitizers for liquid-

Xuejuan Wan received her PhD from the University of Science and Technology of China in 2011. Then, she worked as a Postdoctoral Fellow at Tsinghua University from November 2011 to October 2013. After that, she joined Shenzhen University in November 2013. Now, she is an Associate Professor in the College of Materials Science and Engineering, Shenzhen University. Her research interests focus on conjugated polymer synthesis, printing thin-film solar cells, and luminescent or self-healing polymer materials.

Jiaoning Tang received his PhD from Xi'an Jiaotong University in 1994. He worked at Xiamen University as a Postdoctoral Fellow from 1994 to 1996. Then, he joined Shenzhen University in 1997. He is currently a Full Professor in the College of Materials Science and Engineering, Shenzhen University. His research interests focus on the preparation of nanometer functional materials and new types of energy materials.

Chih-Wei Chu received his PhD degree from the Department of Materials Science and Engineering at the University of California, Los Angeles (UCLA), in 2006. Currently, he is the Deputy Director in the Research Center for Applied Sciences (RCAS) at Academia Sinica. He is a materials scientist with expertise in the fields of thin-film electronics and advanced materials for photovoltaic cells, LEDs, batteries, memory devices, energy saving, conversion, and storage technologies. He has published more than 190 refereed papers with over 13 000 citations (h-index: 53).

Gang Li is a Full Professor in the Department of Electronic and Information Engineering, Hong Kong Polytechnic University (PolyU). Before joining HK PolyU in 2016, he was an Associate Research Professor in the Department of Materials Science and Engineering, UCLA, and VP of Solarmer Energy Inc. in Los Angeles (2007–2011). His research interests are organic polymers and hybrid advanced materials and devices for energy applications. He obtained his BS degree from Wuhan University (Space Physics), followed by MS (Electrical Engineering) and PhD (Condensed Matter Physics) degrees from Iowa State University in 2003. He has been a Thomson Reuter/Clarivate Analytics Highly Cited Researcher since 2014 (Materials Science, 2014–2019; Physics, 2017–2018; Chemistry 2018). He has published over 120 papers with over 56 000 citations (h-index: 69, Google Scholar).

electrolyte-based dye-sensitized solar cells (DSSCs) achieved PCEs of 3.13% and 3.81%, respectively.[19] In 2012, N. G. Park, M. Grätzel *et al.*[20] fabricated solid-state photovoltaic devices using perovskite films as the light-absorbing layers with PCE close to 10%. Although they have attracted global intensive research interest, the PCEs of PSCs still suffer from the poor morphology of the perovskite photoactive layer due to the lack of understanding of the film formation mechanism. In 2014, the pioneering work on the introduction of antisolvent and intermediate phases induced by precursor coordination has been one of the first studies that highlighted the importance of the nucleation and crystal growth of perovskite films in morphology control as well as photovoltaic applications.[21] Later, a large number of reports based on a small area (<0.1 cm^2) by spin-coating fabrication have confirmed that the antisolvent engineering process is an efficient approach to control the perovskite thin-film formation, enabling optimal morphology with uniform and dense surface perovskites, enhanced crystal phase purity, and increased crystallinity, which can yield a reproducible photovoltaic performance.[22–25] Besides the solvent engineering process, other strategies such as gas blowing,[26–30] thermal effect,[31–34] vacuum treatment,[35–37] and additives[38–40] have been innovatively applied to assist the perovskite thin-film formation for achieving optimal morphology, stressing the importance of nucleation and crystal growth control during perovskite film formation.

The PCE of PSCs in small-scale cells (~0.1 cm^2) in laboratory research has seen a surge of progress in the past few years, mainly attributable to the improved chemical composition,[41,42] interfacial contact,[43,44] and optimized morphology[44–46] of perovskite thin films because of innovations in perovskite precursor chemistry and fabrication engineering. Until now, certain key issues have hindered the progress of perovskite photovoltaic technology from real-world applications such as stability and cost; there have been excellent reviews regarding this issue already.[16,47] Among all these issues, one of the most urgent challenges is the technologies and developments addressing the transition from lab-scale PSCs fabrication (such as antisolvent engineering assisting the spin-coating method) to large-area devices by using scalable manufacturing techniques. Intensive efforts have been directed in the past few years with noticeable progress in the scaling-up of PSCs: (i) small-area devices fabricated by scalable casting have already achieved comparable PCE levels to those of spin-coated ones.[48,49] (ii) For large-area PSCs, certified PCE of 17.9% (area > 19 cm^2) for a perovskite module has been recently demonstrated.[50] Meanwhile, scalable deposition approaches combined with suitable nucleation and crystal growth control strategies have been developed, such as high-temperature blading,[51] air-knife-assisted meniscus coating,[48] high-temperature spray coating,[52] and so on. Therefore, it is imperative to investigate solution-processed perovskite film formation mechanism since it plays a critical role in controlling the perovskite film morphology and consequently the photovoltaic performance. An in-depth understanding of the nucleation and crystal growth of perovskite thin films is undoubtedly necessary and can considerably facilitate the scaling-up and commercialization of PSCs.

In this review, we focus on the classical nucleation and crystal growth in addition to related theories; consequently, we show how these diverse strategies have been applied during different fabrication processes to control perovskite thin-film growth, particularly using scalable fabrication approaches. PSC architectures and perovskite photoactive layer deposition methods, including the solution and vapor phases, will be briefly summarized. Thereafter, we systematically compare different scalable deposition methods based on solution processing, including meniscus coating, spray coating, screen printing, and inkjet printing, and we discuss their advantages and limitations in terms of PSC processing and the efforts that have been made to scale-up perovskite photoactive layers. We further discuss the strategies to control the nucleation and crystal growth of perovskite thin films from both the physical aspect (drying kinetics) and perovskite precursor chemistry aspect. Subsequently, we provide essential perspectives on the strategies to understand the control mechanism for perovskite thin-film formation during scalable fabrication processes, aiming at overcoming the key challenges involved in the transfer from laboratory small-size fabrication to scalable large-area manufacturing without sacrificing the quality of perovskite films. Finally, we provide an outlook on the challenges associated with PSC scale-up, focusing on the scalability of processes and materials.

2. Fundamentals of nucleation and crystal growth in perovskites

The perovskite film growth mechanism plays a critical role in the final morphology and consequently the performance of the perovskite device, not only for PSCs but also light-emitting diodes,[53,54] resistive memory devices,[55,56] and photodetectors.[57,58] Therefore, it is imperative to understand the processes of perovskite nucleation and crystal growth that occur during a scalable manufacturing process in order to actually realize potential applications. In this section, we outline classical nucleation and crystal growth in addition to the related theories, summarizing the works related to these theories involving solution-processed perovskite thin films.

2.1 Classical nucleation

In classical nucleation, a monomer implies the minimum subunit of a particle and the basic unit of the growth species. A cluster typically comprises several different monomers. The definition of monomers in the solution state is much more complicated. It may show up in different forms, such as dissociated ions or complexes.[59] Nucleation is the process in which nuclei or seeds with a certain thermodynamic phase act as templates for a crystal to grow.[60] Nucleation occurs when the concentration of the growing species is sufficiently higher than its solubility to reach a supersaturated state. Hence, supersaturation plays an important role as the driving force for nucleation.

For homogeneous nucleation, the nucleation process happens without the need for preferred nucleation sites. It can

be distinguished by the uniform formation of seeds over the entire phase.[61] The total free energy change (ΔG) was determined to thermodynamically investigate the homogeneous nuclei formation process.[59] To simplify the understanding of the nucleation process, the particle shape was defined as a spherical ball. In this case, the total free energy for the spherical particle is the sum of the surface free energy (ΔG_s), namely, free energy between the particle surface and the bulk of the particle, and the bulk (or volume) free energy (ΔG_v), namely, the free energy between a large-sized particle and the solute in the solution. Here, ΔG_s is a positive value, which is proportional to r^2 (r is the radius of the particle); ΔG_v is a negative value proportional to r^3 when the solution reaches the supersaturated state, as shown in Fig. 1a.

Hence, the total free energy can be defined as follows:

$$\Delta G = \Delta G_s + \Delta G_v = 4\pi r^2\gamma + \frac{4}{3}\pi r^3 \Delta G_v \quad (1)$$

where r is the radius of the simulated spherical particles and γ is the interfacial energy or surface energy between the supersaturated solution and crystalline surface.[61] The bulk-free energy (ΔG_v) per unit volume itself (eqn (1)) is dependent on the Boltzmann constant (k_B), temperature (T), degree of supersaturation (S) in the solution phase, and molar volume of the nucleus (v). The degree of supersaturation is defined as $S = C/C_s$, where C is the solute concentration and C_s is the solubility limit ($C > C_s$). Therefore, ΔG_v can be defined as follows:

$$\Delta G_v = \frac{-k_B T \ln(S)}{v} \quad (2)$$

Taking into consideration both ΔG_v (negative value) and ΔG_s (positive value), it can be understood that the nuclei formation process in the supersaturated solution phase directly depends on the critical radius of the nuclei (r^*).[59] That is, when the nuclei have radii smaller than r^*, they get redissolved into the solution; however, when the radii of the nuclei are greater than r^*, they are thermodynamically stable and can exist in the solution, able to grow further. Hence, r^* can be considered as the minimum radius value at which a seed or nuclei can survive in the solution and grow further without being redissolved into the solution.

In real-world experiments, there might be impurities from other phases in the solutions. In the presence of such active centers (walls, impurities, bubbles, and so on), the energy barrier necessary to overcome the occurrence of nucleation is noticeably decreased.[62,63] Hence, different from the homogeneous nucleation process, heterogeneous nucleation usually happens significantly easily at such preferential sites. Since ΔG_s is always positive and ΔG_v is always negative, the maximum free energy necessary to form a stable nucleus can be achieved, allowing further growth. When the free energy reaches the maximum value, $d\Delta G/dr$ should be zero, which yields the critical free energy (ΔG^*). As shown in eqn (1), γ is one of the key factors influencing the nucleation behavior. Among a liquid and two solids in contact, the interfacial energy diagram has three phases, as shown in Fig. 1b. The terms γ_{cl}, γ_{cs}, and γ_{sl} are the interfacial energies between the liquid and crystalline phase, crystalline phase and solid surface, and solid surface and liquid, respectively. Here, θ is the contact angle of the solution on the solid surface. If $\theta < \pi$, the nuclei and active centers exhibit high affinity, leading to a lower energy barrier for nucleation. This phenomenon can be ascribed to the strong reduction in the interface energy. Therefore, the free energy of a heterogeneous nucleation process has been modified by introducing Φ, a factor depending upon θ. This modification makes it equal to that of a homogeneous nucleation process, as defined in eqn (3).

$$\Delta G^*_{hetero} = \Phi \Delta G^*_{homo} \quad (3)$$

The parameter Φ in eqn (3) can be expressed as follows:

$$\Phi = \frac{(2+\cos\theta)(1-\cos\theta)^2}{4} \quad (4)$$

when $\theta = 180^\circ$ (implying no affinity between the solution and solid surface at all), $\cos\theta = 1$, $\Phi = 1$, and $\Delta G^*_{hetero} = \Delta G^*_{homo}$, suggesting that the heterogeneous nucleation critical energy is equivalent to the counterpart of the homogeneous critical energy.

With regard to the solution-based fabrication of perovskite thin films, research reports have emphasized the importance of

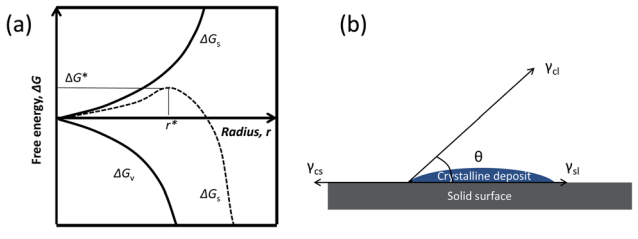

Fig. 1 (a) Explanation of the existence of a "critical nucleus" *via* a schematic diagram using the classical free energy diagram of homogeneous nucleation indicating the existence of a "critical nucleus." (b) Illustration of the contact angle (θ) for heterogeneous nucleation.

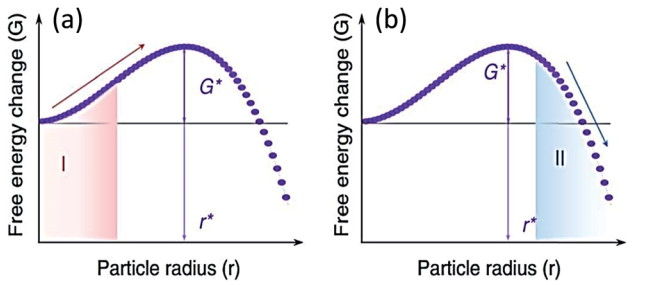

Fig. 2 Evolution of G during the crystallization process without (a) and with (b) the seed crystals. In the absence of seed crystals, a nucleus must first be formed, and the nucleus must then overcome G^* to grow beyond r^* (region I). In the case of perovskite seeds embedded in PbI_2, the size of the seed crystal is already larger than r^* and therefore crystallization spontaneously commences from the seed (region II). Reproduced with permission from (ref. 67). Copyright 2018, Nature Publishing Group.

nucleation control for perovskite film growth.[64–66] Upon classical nucleation, Zhao *et al.*[67] devised a perovskite seeding method that efficiently incorporated cesium and beneficially modulated perovskite crystallization. Perovskite seed crystals were embedded in a PbI_2 film as the perovskite seeds for perovskite crystal growth. Perovskite seeds serve not only as the cesium source but also act as nuclei to facilitate crystallization during perovskite formation. For the traditional two-step method, the crystallization of perovskites cannot happen until the formation of nuclei, for which ΔG^* has to be overcome, as shown in Fig. 2a (region I). In contrast, for the perovskite seed growth method, perovskite growth immediately occurs from the perovskite seeds (nucleation centers) when the alkylammonium halide salts are coated on top of the PbI_2 thin film, as shown in Fig. 2b (region II).

2.2 Classical crystal growth

The growth of nanoparticles is dependent on two mechanisms: surface reaction and monomer's diffusion to the surface.[59] To explore the crystal growth controlled by diffusion, Fick's first law,[68] as shown in eqn (5), can be applied. In eqn (5), J denotes the flux of growing monomers moving through the proposed spherical plane, D stands for the diffusion coefficient, x is the distance from the top surface of the seed crystal, and C is the growing species concentration at distance x.

$$J = 4\pi x^2 D \frac{dC}{dx} \tag{5}$$

For the growth process of crystals in the solution state, Fick's first law can be defined as follows:

$$J = \frac{4\pi D r(r+\delta)}{\delta}(C_b - C_i) \tag{6}$$

where δ is the distance from the bulk concentration of growth species within the solution to the solid particle surface, C_i is the concentration of growth species at the liquid/solid interface, and C_b is the bulk concentration of growing species within the solution. The diffusion region is the region where the concentration gradient is visible, as shown by the shaded area in Fig. 3a.

Given that J is a constant, irrespective of x due to the steady state of the diffusion process of the growth species, the integration of $C(x)$ from $(r + \delta)$ to r yields eqn (7):

$$J = 4\pi D r(C_b - C_i) \tag{7}$$

A similar equation can be obtained for the rate of the surface reaction rate "k" in eqn (8). Ideally, the rate is assumed to be independent of the dimensions of particles in the solution.

$$J = 4\pi r^2 k(C_b - C_i) \tag{8}$$

From eqn (7) and (8), it is evident that there are two key limiting factors for the crystal growth process: (1) the diffusion process of monomers toward the surface or (2) the rate of the reaction speed of these growth species at the surface. If the diffusion process is the dominant limiting factor, the change in particle size with time can be expressed as follows:

$$\frac{dr}{dt} = \frac{Dv}{r}(C_b - C_r) \tag{9}$$

where C_r is the concentration of growth species at distance r to the crystal surface.

Similarly, if the surface reaction rate is the main limiting factor, then eqn (7) and (8) can yield eqn (10):

$$\frac{dr}{dt} = kv(C_b - C_r) \tag{10}$$

When the growth of the nucleus is controlled neither by diffusion nor by surface reaction,[69] the increase in the particle's radius becomes more complicated; details from the mathematical perspective have been provided elsewhere.[70]

There have been reports exploring the different strategies used to control perovskite growth, making considerable progress for the growth of high-quality perovskite thin films. Here, we briefly show two examples for understating perovskite growth, guided by the fundamentals of classical crystal growth.

In the first example, from a fundamental point of view, we explore the perovskite film growth mechanism for coating and growth at room temperature. Experimental results reveal that perovskite crystal growth is a diffusion-controlled process.[48]

Fig. 3a and b show the concentration of growing species as a function of distance to the crystal surface. According to the classical crystal growth theory, diffusion-controlled growth can be easily distinguished by a noticeable concentration gradient between the crystal surface and bulk solution, *i.e.*, the diffusion region. Fig. 3c shows the top-view SEM images of a perovskite intermediate solid film dried by air blowing during its growth process. Evidently, a big-size domain is seen to be surrounded by the diffusion layer. Fig. 3d–f show perovskite nucleation and growth in a natural slow-drying case. In the early stages, the dimensions of the solid seed of the initial precursor were relatively small, and the diffusion layers of the neighboring domains were almost independent (without any overlap). This yields an almost isotropic growth, as shown in Fig. 3d. The growth of perovskite seeds narrows the distance between the neighboring crystal surfaces, resulting in an overlapping of the neighboring regions in the diffusion layer. Due to the lack of growing species in the overlapped region, it eventually leads to a poorly covered area on the substrate. Meanwhile, the neighboring perovskite seeds finally grow in an anisotropic manner (Fig. 3f).

In another study, Lin *et al.* investigated perovskite ($FA_{0.85}MA_{0.15}PbI_{2.55}Br_{0.45}$) growth kinetics with the help of real-time optical microscopy measurements fabricated by the meniscus-assisted solution printing strategy at an elevated temperature, aiming at exploring the crystallization mechanism.[51] Two-stage crystal growth was observed: initially, there was a quadratic increase in the crystal island followed by a linear increase in the crystal area. They have quantified perovskite crystal island growth as a function of time upon the scaling of the capture zone model,[71,72] where crystal growth is mainly controlled by

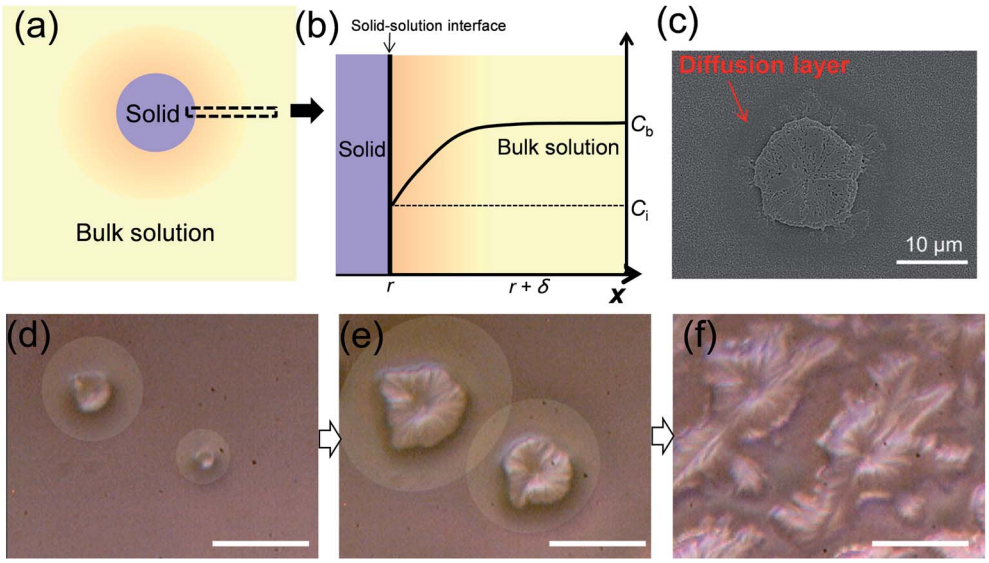

Fig. 3 (a) Schematic explanation of the diffusion layer. (b) Perovskite precursor concentration as a function of distance x away from the solid surface. (c) Top view of the SEM image of perovskite intermediate film quenched by air blowing. (d–f) Snapshots of *in situ* optical microscopy for perovskite nucleation and growth scale bar: 20 μm. Reproduced with permission from (ref. 48). Copyright 2019, Wiley-VCH Verlag GmbH & Co. KGaA, Weinheim.

both monomer diffusion length and accessible collection area. With the help of a Voronic cell, which defines the monomers closer to a specific cell than that to any neighboring one,[73] the accessible collection area of the crystal island of $FA_{0.85}MA_{0.15}PbI_{2.55}Br_{0.45}$ can be estimated. The central point of each perovskite crystal island was labeled as the nucleation center in the Voronoi cell diagram (Fig. 4a and b).

In the initial growth stage, the center of the $FA_{0.85}MA_{0.15}PbI_{2.55}Br_{0.45}$ perovskite crystal is labeled as P, as shown in Fig. 4a. The effective radius (R_{eff}) of the perovskite island was small at time t_0 as compared to the Voronoi cell radius (R_{Vor}) of the same perovskite crystal island since it was relatively far from the neighboring perovskite islands. In this case ($R_{eff} + \delta < R_{Vor}$), the crystal growth rate was mainly determined by δ with quadratic crystal growth. This can be illustrated by $dA/dt = k_q(2\pi\delta R_{eff} + \pi\delta^2)$, where k_q is the rate constant and A (πR_{eff}^2) is the island area.[73] As the perovskite crystal island grows, increased R_{eff} leads to $R_{eff} + \delta > R_{Vor}$. Further, additional new adjacent crystals emerge, as shown in Fig. 4b. The labeled island has to compete with these neighboring crystals for their growth species to grow further. Hence, the perovskite crystal growth rate was mainly determined by the accessible collection area, yielding linear crystal growth.

2.3 Theories of nucleation and crystal growth

Within this section, we summarize the different theories for the nucleation and growth and their applications in the perovskite thin-film formation process.

2.3.1 LaMer mechanism. The crystal growth can be categorized into the following two types. (a) Diffusion-controlled growth: when the concentration of the growth monomers decreases to a value lower than that of the minimum critical concentration necessary for nucleation, the crystal growth continues, but nucleation stops. (b) Surface-process-controlled growth: when the diffusion of the growth species from the bulk to the growth surface is sufficiently rapid, the growth rate is controlled by the surface process. LaMer[74] studied the synthesis of sulfur sols with regard to the decomposition of sodium thiosulfate and found that it comprised two steps: (1) formation of free sulfur from the thiosulfate and (2) formation of sulfur sols in solution. The so-called LaMer mechanism[75] conceptually separated nucleation and growth into two steps, and the growth process was proposed to be controlled by the diffusion of the growth species. He correlated the degree of supersaturation of the solution with crystal nucleation and growth, which are the critical factors that determine the film formation mechanism and consequently the film morphology.

For nucleation and growth from the solution state, a traditional LaMer curve comprises three portions: (i) increase in the monomer concentration in the solution; (ii) "burst nucleation" in the solution caused by the monomer concentration over the minimum supersaturation limit (C^*_{min}); and (iii) nucleation growth process controlled by the diffusion of growing species. These three stages are shown in Fig. 5, where the concentration of monomers is schematically plotted as a function of time.

On the basis of the LaMer mechanism, different perovskite film morphologies from different drying kinetics have been systematically explored in our earlier work. The air-knife-modified meniscus coating technique was applied, which can significantly accelerate the evaporation rate of the solvent molecules (Fig. 5a). This can rapidly induce the oversaturation stage in the initial solution, yielding a higher degree of supersaturation. Eventually, it can lead to a much higher rate of crystal nucleation (quantitative analysis is explained in the

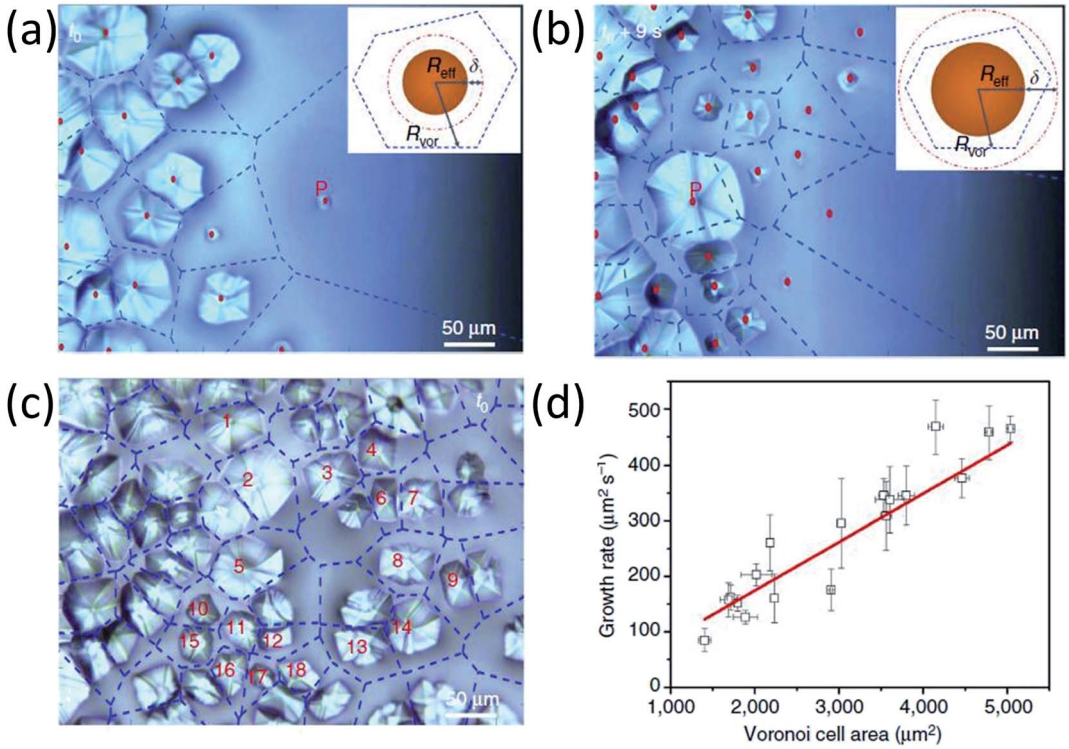

Fig. 4 (a) Voronoi cell diagram of perovskite islands at time t_0. For the tracked perovskite island, the center is labeled P. Inset shows the topological relationship, $R_{eff} + \delta < R_{Vor}$, where R_{eff} is the effective radius of the perovskite island, δ is the solute diffusion length, and R_{Vor} is the effective radius of the corresponding Voronoi cell. (b) Voronoi cell diagram of perovskite islands at time t_0 + 9 s. For the tracked perovskite island, the center is labeled P. Inset shows the topological relationship, $R_{eff} + \delta > R_{Vor}$. (c) Eighteen selected perovskite islands and the corresponding Voronoi cells for tracking the perovskite crystal growth rate as a function of the Voronoi cell area for each crystal island from time t_0' to t_0' + 3 s. (d) Plot of the average growth rate of 18 perovskite crystal islands as a function of their Voronoi cell areas. Error bars denote the standard deviation of the data collected from time t_0' to t_0' + 3 s. Reproduced with permission from (ref. 51). Copyright 2017, Nature Publishing Group.

subsequent section, where the von Weimarn theory is used). Subsequently, nitrogen blowing resulted in an enhanced nucleation density (inset, Fig. 5b). Hence, for the considerably lower degree of supersaturation of the natural drying case with reduced nucleation density, it ultimately led to the growth of larger-sized domains (Fig. 5c). On the other hand, high-speed laminar air-knife nitrogen blowing yields a remarkably smaller cluster size (Fig. 5c). Further, nitrogen blown at the intermediate stage is shown by the blue curve in Fig. 5b. These different perovskite film growth mechanisms effectively match the final morphology (Fig. 5d and e), as per the LaMer mechanism.

Hu *et al.*[76] explored perovskite (methylammonium lead triiodide, $MAPbI_3$) crystallization and microstructure evolution at different coating temperatures by using *in situ* characterization tools, such as X-ray scattering and optical microscopy. Different from polymeric spherulites derived from the radial growth of crystalline lamellae, banding in the perovskites are closer to Liesegang rings, which can be attributed to a periodic precipitation reaction. The periodic patterns, as observed in the $MAPbI_3$ perovskite crystallization (Fig. 6a), can be attributed to the complex interplay among the solution flow, solvent extraction, solute diffusion, and crystal growth. When the perovskite precursor solution is cast onto a heated substrate, the evaporation of the solvent molecules becomes more rapid. Once the solution reaches the minimum supersaturation limit, nucleation occurs, followed by crystal growth. The schematic diagram of nucleation and growth as a function of time on the basis of different processing temperatures is shown in Fig. 6b. The *in situ* microscope images of the perovskite films formed at 100 °C are shown in Fig. 6c.

2.3.2 von Weimarn theory. In early 1925, based on the summarization of experimental data, von Weimarn proposed a relationship between the initial supersaturation and the average size of aggregates of a newly emerged phase formed in the course of the nucleation processes in the system.[77] Since then, his empirical rules have become an integral part of crystal growth theories.[78–80] In short, the first von Weimarn rule claims that the average crystal size measured after the crystallization process increases when the initial relative supersaturation drops. The second rule proposes that within a given crystallization time, the average crystal size exhibits a decreasing trend as a function of the initial relative supersaturation. As compared to the second rule, the first rule is more popular and compatible with modern theories.[79]

According to these von Weimarn rules, crystal nucleation and growth are strongly dependent on the supersaturation degree. It has been concluded that the competition between

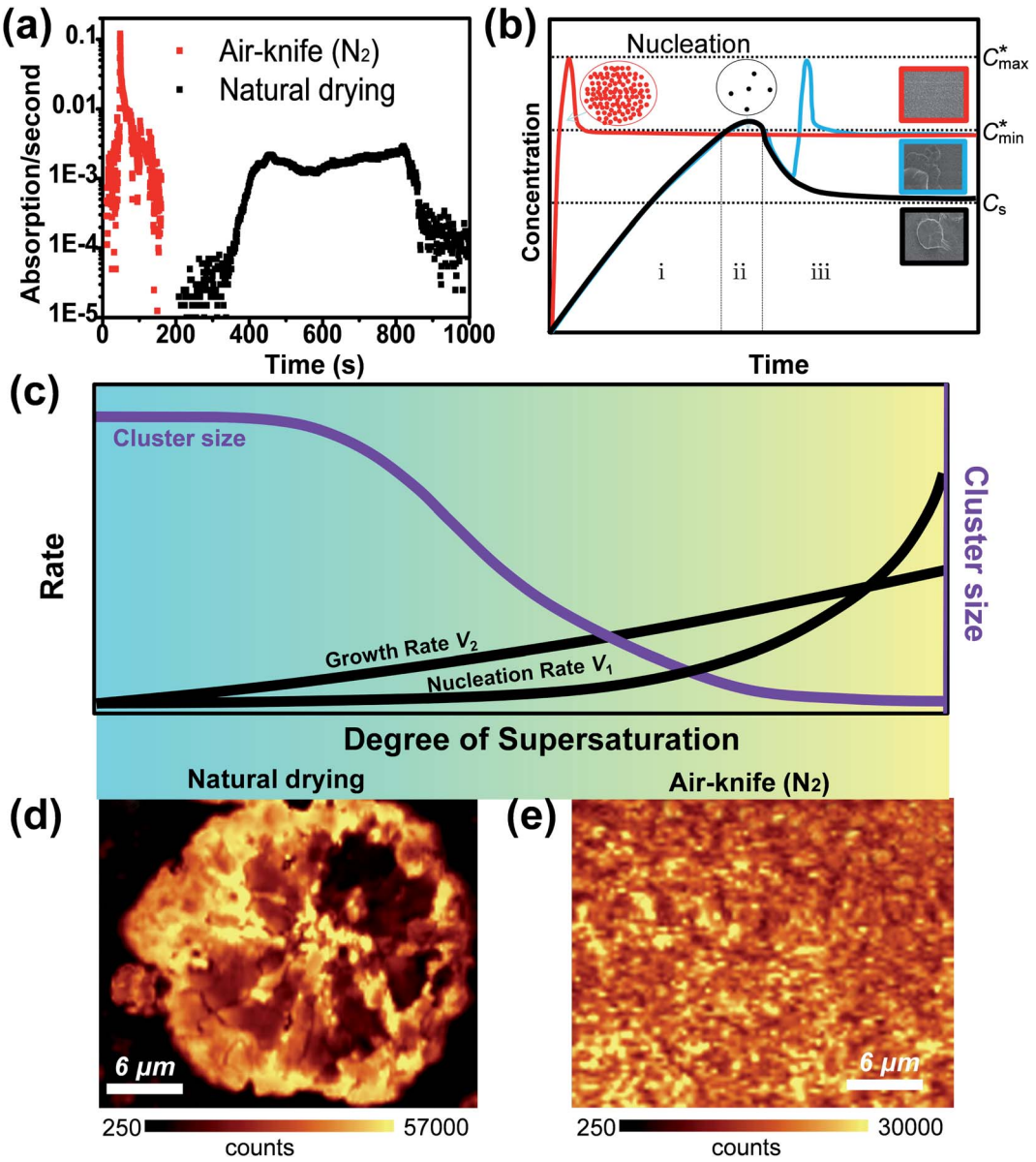

Fig. 5 (a) Quantifying the different drying rates with the first derivative of the time-resolved absorbance at 500 nm. (b) Nucleation and crystal growth of the perovskite film for three cases: nitrogen blown in the solution state (red line), natural drying (black line), and nitrogen blown in the intermediate phase (blue line) in the classical LaMer model. (c) Quantitative nucleation and growth rates as a function of the degree of supersaturation, and the corresponding grain cluster size. (d and e) Photoluminescence mapping of a natural drying perovskite film as well as the air-knife nitrogen-blown-quenched perovskite film. Reproduced with permission from (ref. 48). Copyright 2019, Wiley-VCH Verlag GmbH & Co. KGaA, Weinheim.

crystal nucleation and growth can directly determine the average dimensions of the crystal clusters. The von Weimarn rules nucleation rate[77] can be defined as

$$V_1 = kA \exp\left(\frac{-\Delta G^*}{k_B T}\right) \quad (11)$$

where k is a constant, k_B is the Boltzmann constant, T is the absolute temperature, and A is the complicated function of the molecular-level diffusion kinetics parameters. Further, ΔG^* is the critical free energy of nucleation. For a spherical perovskite cluster,[81] it is defined as

$$\Delta G^* = \frac{16\pi\gamma^2\Omega^3}{3k_B{}^2T^2\sigma^2} \quad (12)$$

where γ is the surface free energy of the critical cluster, Ω is the perovskite molecular volume of the crystal, and σ is the degree of supersaturation of the perovskite precursors. Based on eqn (11) and (12), V_1 exhibits an exponential growth rate with the degree of supersaturation, *i.e.*, $V_1 \propto \exp(-1/\sigma^2)$. With the help of Burton–Cabrera–Frank theory,[68] V_2 can be quantitatively correlated with supersaturation σ: parabolic growth occurs ($V_2 \propto \sigma^2$) when the degree of supersaturation is low and linear growth ($V_2 \propto \sigma$) occurs when the degree of supersaturation is high.[81] In

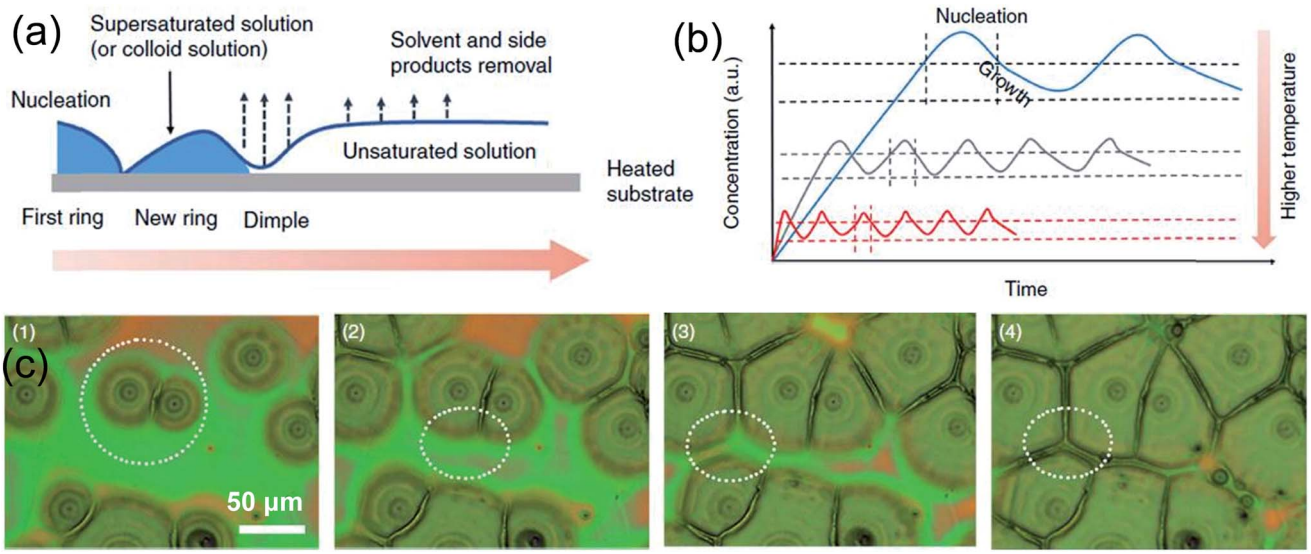

Fig. 6 (a) Schematic of periodic and rhythmic crystallization. (b) Schematic of nucleation and growth with respect to time based on different temperatures. (c) Select *in situ* microscopy images of perovskite films heated at 100 °C. The interval time is 0.02 s. Reproduced with permission from (ref. 76). Copyright 2017, Nature Publishing Group.

contrast to the crystal growth rate V_2, V_1 is more sensitive to the degree of supersaturation. For the number of clusters per unit area (N), it is inversely proportional to the average size of the crystal cluster, which can be expressed as[81]

$$N = 1.1\left(\frac{V_1}{V_2}\right)^{1/2} \quad (13)$$

2.3.3 Ostwald ripening. The Ostwald ripening phenomenon was first explained in 1900.[82] The driving force for this growth process can be ascribed to the change in the solubility of growth species, which depends on their size; it is quantitatively described by the Gibbs–Thomson relationship.[59] The smaller size of the growth species is associated with higher surface energy and solubility; therefore, these species are prone to redissolution in the solution and redeposition of the dissolved species on the surface of larger particles, allowing the existing larger-sized particles to grow further. As a result, the concentrations of the growth species are usually reduced during the Ostwald ripening process and the average size of the growing particles increases. On the basis of the Ostwald ripening data, Lifshitz *et al.*[83] provided a systematical mathematical theory with the assumption of a closed system.

The Ostwald ripening mechanism has also been applied to explain the grain growth in perovskite thin films *via* coalescence.[84–86] For solution-processed perovskites, it has been recently reported that residual solvent molecules embedded in perovskite intermediate films play a critical role in the dissolution–recrystallization process of perovskite grains during thermal annealing treatments.[87] This significantly enhances the Ostwald ripening effect. It has been reported that perovskite precursor films can release the residual solvent molecules and then get converted into perovskites. Meanwhile, the small-size perovskite grains get dissolved in the emitted solvent molecules, which then recrystallize into larger neighboring grains, yielding perovskite grain coarsening *via* Ostwald ripening.

Different from traditional Ostwald ripening in perovskite materials, Pham *et al.*[85] reported a simple method to reduce the grain boundaries and to passivate the surface of a $MAPbI_3$ film by guanidinium thiocyanate (GUTS)-assisted Ostwald ripening posttreatment. This process yielded a high-optoelectronic-quality $MAPbI_3$ film comprising micron-sized grains, which were much larger than those in the control sample, as shown in Fig. 7a and b. The schematic illustrations of the traditional Ostwald ripening process and GUTS-assisted Ostwald ripening process are shown in Fig. 7c.

3. Device architecture and perovskite photoactive layer deposition

3.1 Perovskite solar cell architectures

The typical device architectures of PSCs can be categorized into three types: regular mesoporous (n–i–p) structure, regular planar (n–i–p) structure, and inverted planar (p–i–n) structure.[88] The regular configuration of PSCs is transparent conductive oxide (TCO)/electron transport layer (ETL)/perovskite-absorbing layer/hole transport layer (HTL)/top electrode. Regular mesoporous architecture was adopted from DSSCs, which was the first structure applied in PSCs; thereafter, the latter two architectures were developed. Generally, a mesoporous PSC comprises an ETL scaffold with a nanoscale porous structure. Then, the perovskite photoactive layer covers the scaffold, yielding a compact and continuous capping layer. Since the perovskite layer penetrates into the ETL scaffold, a well-intermixed structure can be formed between the perovskite-absorbing layer and ETL. The fabrication of regular mesoporous PSCs finishes with the sequential deposition of HTL and the top electrode. It has been reported that the mesoporous

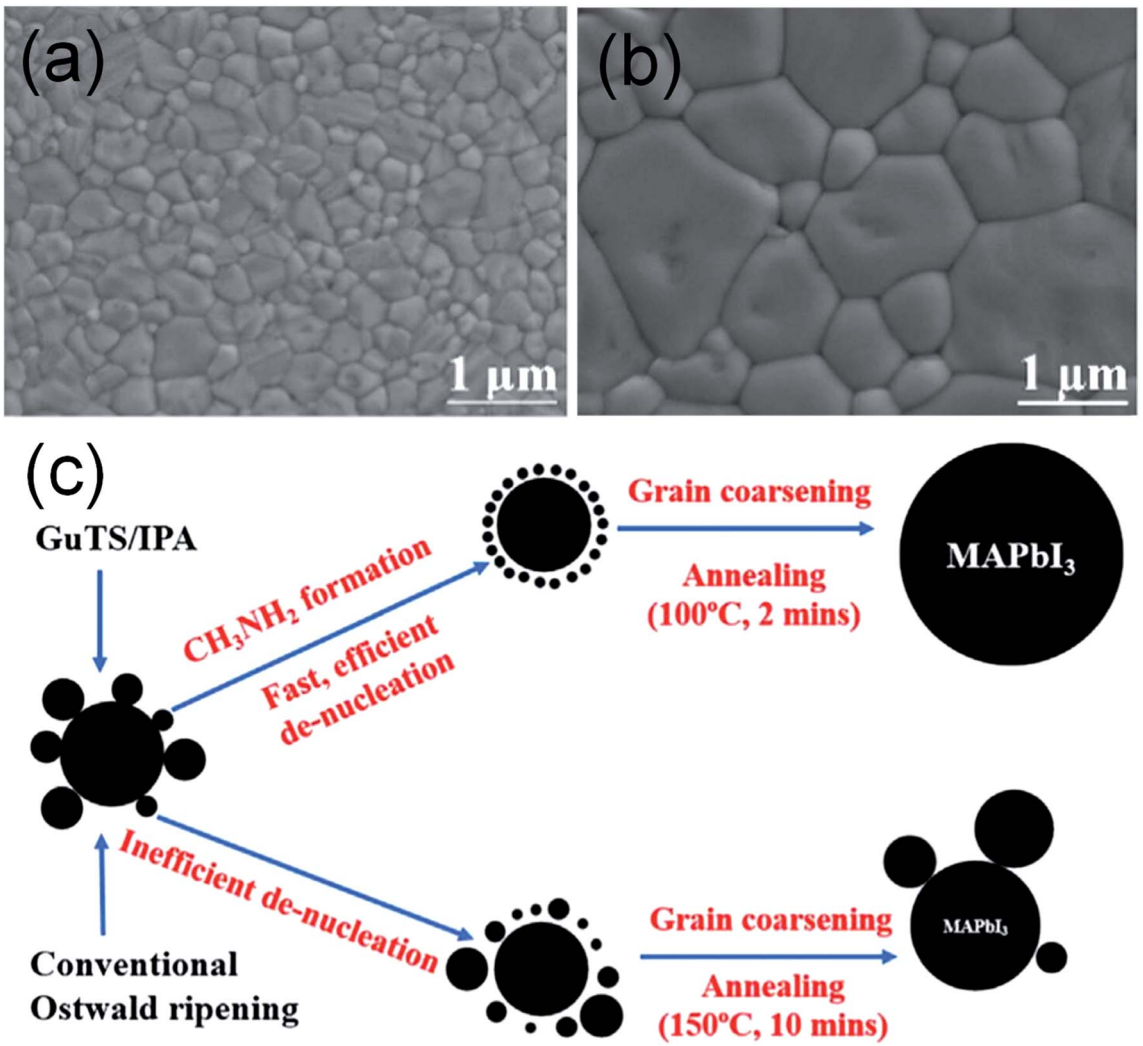

Fig. 7 Top-view SEM images of $MAPbI_3$ films. (a) Control $MAPbI_3$ film and film treated with different concentrations of GUTS/IPA solution (b) at 4 mg mL^{-1}. (c) Schematic illustration of the Ostwald ripening process for $MAPbI_3$ perovskite crystal growth assisted by GUTS in this work and by a conventional method. Reproduced with permission from (ref. 85). Copyright 2017, Elsevier Inc.

layer with effective intermixing between the perovskite layer and ETL can facilitate charge separation and efficiently suppress the notorious photocurrent–voltage hysteresis in PSCs.[21] The highest PCE of 23.3% (ref. 89) has been obtained with this regular mesoporous architecture. Initial works involving PSCs were mainly based on the regular mesoporous structure and the latter two structures emerged as the evolution of PSC architectures, also exhibiting outstanding photovoltaic performances.

The regular planar (n–i–p) architecture comprises a compact ETL layer; it can be distinguished from the regular mesoporous architecture as it features perovskite–ETL-intermixed layers. Although it has been reported that PSCs with a regular planar structure are more likely to suffer from photocurrent–voltage hysteresis, recent research efforts involving the ETL/perovskite interface have led to the fabrication of regular planar PSCs with improved photovoltaic performances and negligible hysteresis.[90–92] As compared to the regular mesoporous PSC structure, regular planar PSCs have achieved almost the same level of or even better device photovoltaic performance. Although certain studies have claimed that a regular mesoporous structure can enhance device stability,[93,94] a systematical stability comparison remains to be confirmed. On the other hand, from the aspect of the ETL process, a mesoporous ETL layer has to add one more step to fabricate a mesoporous structure at a considerably higher temperature, which may not be favorable for scalable manufacturing.[88]

Planar p–i–n PSC architecture is typically referred to as an inverted structure since the carrier extraction layers are inverted with respect to regular n–i–p PSC structures. Devices with p–i–n architecture are often constructed with a typical planar structure with a compact HTL, namely, PEDOT:PSS, NiOx, and polymer PTAA.

3.2 Perovskite layer deposition

A perovskite layer functions as the light-absorbing layer in the PSCs; it plays the central role in the performance of PSCs.

Tremendous efforts have been focused on the deposition approaches of perovskite layers for scaling-up of PSCs.[95–99] Besides the widely used solution-casting methods, other approaches have also been applied for perovskite photoactive layer deposition, such as vapor-phase deposition,[100,101] electrodeposition,[102,103] and so on.

3.2.1 Vapor-phase deposition. The vapor-phase deposition technique is commonly used in the fabrication of thin-film solar cells. The already commercialized thin-film photovoltaic technologies, such as copper indium gallium selenide (CIGS) or cadmium telluride (CdTe), heavily rely on physical vapor deposition (PVD).[104,105] The doping of silicon is also realized *via* chemical vapor deposition (CVD).[106] PVD apparatuses for the large-scale fabrication of commercialized thin-film solar cells in the industry have been successfully developed, and this experience and equipment are ready to be translated into PSC fabrication.[88]

The vapor deposition used in perovskite film fabrication includes vapor–solid reaction,[107] dual-source co-evaporation technology,[108] and vapor-assisted methods.[109] The first CVD method developed for the deposition of perovskite materials was based on the vapor–solid reaction technology, which involved the reaction of PbI_2 thin films with MAI vapor.[110] Later, more CVD systems were developed and applied in perovskite materials with different chamber configurations and designs, environmental pressures, reaction temperatures, and organic halide sources.[111–113] Dual-source co-evaporation technology has been successfully applied in perovskite film deposition, yielding decent photovoltaic performance. During the dual-source co-evaporation process, both PbI_2 powders and MAI powders were separately made as the target source and preheated to ~116 and ~325 °C, respectively, to form perovskite films on the substrate. Upon applying this approach, PSCs with PCE >15% have been fabricated.[108]

Although the vapor-phase deposition process possesses the potential to be applied in perovskite thin-film deposition over large scales, these methods often demand the use of more expensive and sophisticated vacuum equipment and relatively long processing times, which could seriously hinder their applications in the low-cost fabrication of PSCs, contradictory to the motif of PSCs.

3.2.2 Electrodeposition. Electrodeposition is another scalable, low-cost, and mature industrial technique for preparing high-throughput mechanical or functional coatings *via* electrochemical reduction or oxidation. It has been widely applied in thin-film solar cells technologies, such as $CuInSe_2$,[114,115] CdTe,[116,117] CIGS,[118,119] and Cu_2ZnSnS_4.[120,121] Until now, several papers[103,122] have reported perovskite thin-film fabrication *via* electrodeposition. It generally comprises two steps: first, PbO_2 or PbO is electrodeposited on a conducting substrate; second, lead oxide is then converted into the perovskite phase through the reaction with organic halides[123] or reaction with HI acid first in order to form PbI_2, which is then converted into a perovskite.[124,125]

The advantage of electrodeposition is the use of a nontoxic solvent in the fabrication process, which is compatible with a broad range of complex-shaped substrates (including flexible ones). However, more efforts are needed to optimize the entire process to achieve a comparable photovoltaic performance.

3.2.3 Solution deposition. Although vapor-phase deposition or electrodeposition has the potential to be used to deposit perovskite thin films over large areas, these methods usually require more sophisticated equipment and more complicated procedures, impeding their application in the low-cost fabrication of PSCs. In contrast, solution-processed perovskite films are more compatible with low-cost scalable printing manufacturing processes; meanwhile, all the record photovoltaic performance in PSCs have been demonstrated when solution processing has been used.

3.2.3.1 One-step deposition. One-step deposition refers to the direct coating of a perovskite precursor solution, which is then converted into the perovskite phase. Due to the easy formation of perovskite aggregates from the precursor solution, the control over film formation is a formidable challenge during the one-step deposition process. It has to be mentioned that since a fairly long time, initial pure $MAPbI_3$ perovskite solar cell devices have been suffering from poor photovoltaic performance, mainly due to the poor coverage of the perovskite thin layer that is obtained by the one-step method. Considerable efforts from different aspects (including precursor solution chemistry, strategies for nucleation and crystal growth control, such as antisolvent dripping, gas blowing, *etc.*) have been expended toward resolving this problem in laboratory research on the basis of a simple spin-coating method. Now, most of the current studies on PSCs *via* the one-step spin-coating approach can yield a continuous and compact perovskite thin film. High-quality pinhole-free uniform perovskite films and excellent solar cell performance have been achieved, yielding well-controlled crystal growth.

However, spin coating is limited to the fabrication of non-scalable solution-processed PSCs. It is, therefore, fairly exciting and necessary to transfer this one-step solution casting to other scalable deposition technologies for its application. A detailed discussion regarding this has been performed in the subsequent chapters.

3.2.3.2 Two-step deposition. By using the solution processing method, perovskite thin films can also be deposited through a two-step deposition route. Namely, a lead halide thin film is initially cast and then converted into a perovskite by reacting with the subsequent solution-deposited organic halide salts.[126] As compared to the direct coating of a perovskite (for example, $MAPbI_3$, one-step deposition) precursor, two-step deposition can be applied to fabricate more compact films over a larger scale since it is easier to deposit uniform PbI_2 thin films than perovskite thin films over a larger area. In the second step, the volume expansion that accompanies the conversion of PbI_2 into the perovskite can fill the pinholes in the thin film, alleviating the complications of morphology control that mar one-step deposition, particularly with scalable deposition processes.[127–129] Moreover, it has been reported that two-step deposition exhibits increased processing tolerance to a humid environment[130,131] as compared to that with the one-step deposition method. One drawback of the two-step deposition method is the variable and long reaction times required to

convert lead halide into a perovskite. In an early work involving the two-step deposition process, the lead halide films were usually dipped in an organic halide solution for a certain amount of time (typically greater than 10 min), and it was reported that the consequent formation of a mesoporous scaffold structure could facilitate organic halide penetration for a faster reaction between the organic halide salt and lead halide.[132] Meanwhile, the addition of Lewis base additives could also accelerate the rate of reaction between the lead halide film and organic halide. For instance, it has been reported that the adduct formation between PbI_2 and DMSO increased the reaction rate of PbI_2 with FAI through an intramolecular exchange mechanism: DMSO in the PbI_2–DMSO adduct readily exchanged with FAI, facilitating the incorporation of FAI and therefore speeding up the conversion into the perovskite.[133]

4. Approaches for scaling-up of solution-processed PSCs

To deposit perovskite thin films through one-step solution processing, organic halides and lead halides were first dissolved in organic solvents (such as *N*,*N*-dimethylformamide (DMF), dimethyl sulfoxide (DMSO), or γ-butyrolactone (GBL)). Although one-step spin coating in laboratory research has been repeatedly demonstrated as an effective way to fabricate high-quality perovskite films with excellent photovoltaic performances, it is still limited to being a small-scale fabrication process. Moreover, a large portion (>90%) of the precursor solution is wasted in this process, which is contradictory to the low-cost motivation of PSCs. In the spin-coating process, thinning and smoothing of the wet-solution films rely on the constant centrifugal force imparted by the spinning process, which is difficult to transfer into a scalable deposition process. Further, the top-performing PSCs fabricated by the one-step spin-coating method are subsequently treated by antisolvent dripping to control the nucleation and growth processes, which cannot be applied in scalable processing. Therefore, intensive effort has been directed toward the aspect of processing strategies to control the perovskite film formation mechanism in scalable deposition methods to achieve comparable photovoltaic performance to that of the counterpart obtained by spin coating. By improving the understanding of factors that influence perovskite thin-film formation, increasing the control of thin-film formation in different deposition processes is necessary and crucial for the scaling-up of PSCs.

4.1 Scalable solution deposition methods

The development of scalable fabrication technologies for fabricating halide PSCs is a formidable challenge for realizing their commercialization potential. In particular, continuous solution coating processes are needed to produce scalable large-area PSCs. Until now, scalable solution deposition methods for perovskite thin films include, but are not limited to, meniscus coating (blade coating, wire-bar coating, slot-die coating), spray coating, inkjet printing, and screen printing. In this section, we briefly compare these scalable deposition methods along with their application in PSCs.

4.1.1 Meniscus coating. Although many papers have distinguished blade coating, wire-bar coating, and slot-die coating as different scalable fabrication methods on the basis of equipment configurations and ink supply systems, they are principally fairly similar techniques—a meniscus[134,135] is first formed by the capillary force across the substrate and then the relative movement yields the coverage of the full wet film on the substrates underneath.

4.1.1.1 Blade coating. Blade coating (Fig. 8a) is a widely used scalable solution-coating technique in the printing industry, particularly in the initial testing of ink coatings. In printable electronics, initially, it has been widely applied for optoelectronic material deposition, such as organic thin-film transistors (OTFTs),[136,137] organic light-emitting diodes (OLEDs),[138,139] organic solar cells (OSCs),[140,141] *etc.* In the blade coating deposition technique, a blade is applied to spread the loaded precursor solution along a moving substrate to form wet solution films. The film thickness is generally determined by several factors, including the ink concentration, surface energy of the substrate, gap between the blade and substrate, and coating speed. This technique can be adapted for continuous fabrication and is compatible with roll-to-roll setups for future massive manufacturing processes expected in the industry. Unlike the spin-coating process, the materials usage is almost 100% with negligible waste, particularly in a continuous roll-to-roll deposition setting. It is noteworthy that the blading process yields a uniform wet film from the precursor solution *via* one-step deposition; the quality of the final solid film is strongly dependent on the applied external processing strategies. For example, both the elevated substrate temperature[49] (Fig. 9) and gas blowing[48] have been reported as efficient strategies to control the perovskite film formation, yielding high crystallinity and pinhole-free perovskite films, with reported PCEs exceeding 20% for both these methods.

Blade coating has also been applied in the two-step deposition method for perovskite film fabrication, particularly for PbI_2 film deposition. For example, Razza *et al.*[142] reported a scalable process for the two-step deposition of $MAPbI_3$ perovskite thin films with the PbI_2 layer coated by blade coating. Air is blown at a high temperature (100 °C) and it was used to control the crystallization of the PbI_2 film by accelerating the evaporation of the solvent molecules. The compact and smooth PbI_2 film was then converted into a perovskite after dipping into a MAI solution with IPA as the solvent. As compared to the one-step deposition method, the two-step sequential deposition method still necessitates the dripping process, which complicates the fabrication process and it is more challenging to control.

4.1.1.2 Wire-bar coating. For the wire-bar coating process (Fig. 8a), a wire-wound bar (a stainless steel rod around which a stainless steel wire is tightly wrapped) is applied to form the meniscus instead of a blade (as used in the blade-coating method).[143,144] The wound wire creates a thread that is always of the same profile. The wire size is determined by the diameter of the wire wrapped around the bar and it is a key parameter to

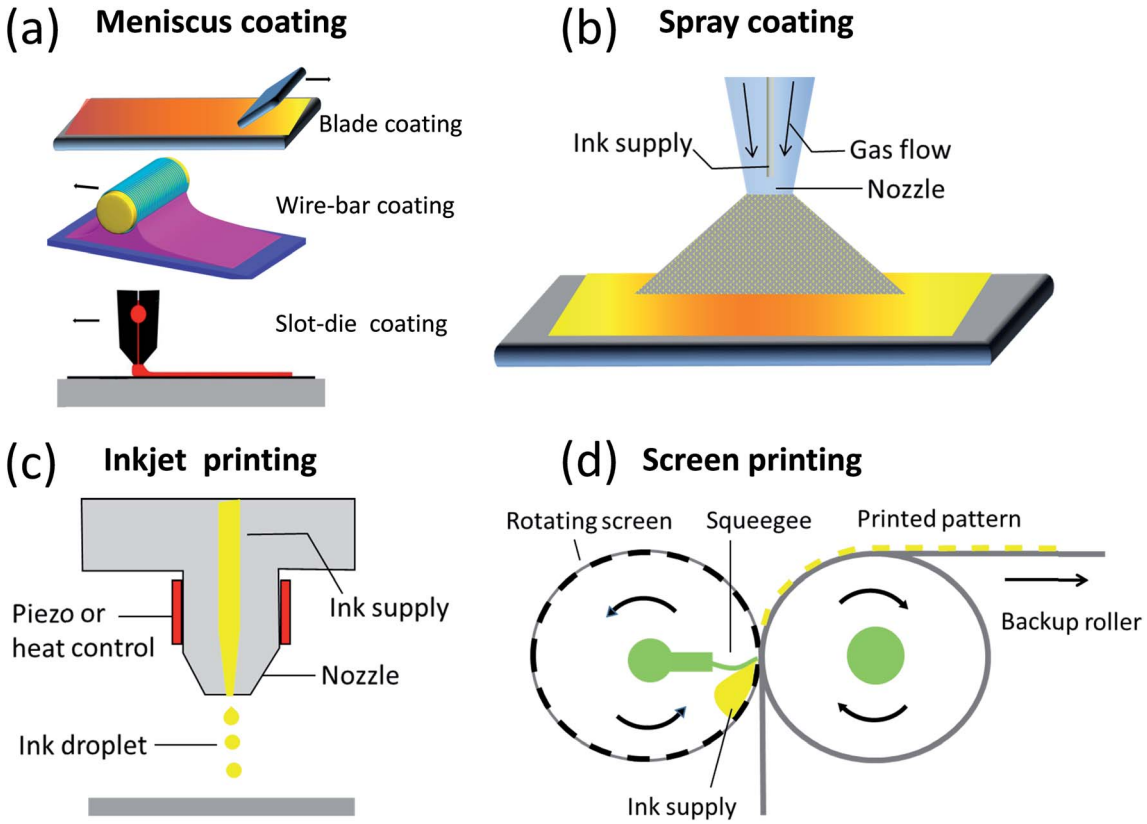

Fig. 8 Common scalable solution deposition methods for the fabrication of PSCs: (a) meniscus coating (blade coating, wire-bar coating, slot-die coating); (b) spray coating; (c) inkjet printing; and (d) screen printing.

determine the amount of coating solution. A solution meniscus forms between the moving wire bar and the stationary substrate after casting the solution, which gradually dries. Similar to blade coating, the thickness and uniformity of the coating layer are determined by the viscosity and concentration of the ink, surface energy of the substrate, gap between the wire bar and substrate, coating speed, *etc*. For wire-bar coating, the configuration of the wire bar, as well as its diameter, plays an essential role in determining the final thickness.[145] Wire-bar coating works well at high coating speeds without experiencing "hydroplaning" effects, which can avoid the formation of nonuniform morphology during coating. It is, therefore, widely considered as a well-controlled and accurate industrial coating method with multiple wire configurations.[146,147] Wire-bar coating has been previously used to coat an active layer in OTFTs[148,149] and flexible OLEDs,[150] and it has also been used to fabricate transparent carbon nanotube electrodes.[151] Y. Ju *et al.*[152] reported a wire-bar coating process that introduced an intermediate phase for a large area with smooth film morphology and complete coverage using *N*-cyclohexyl-2-

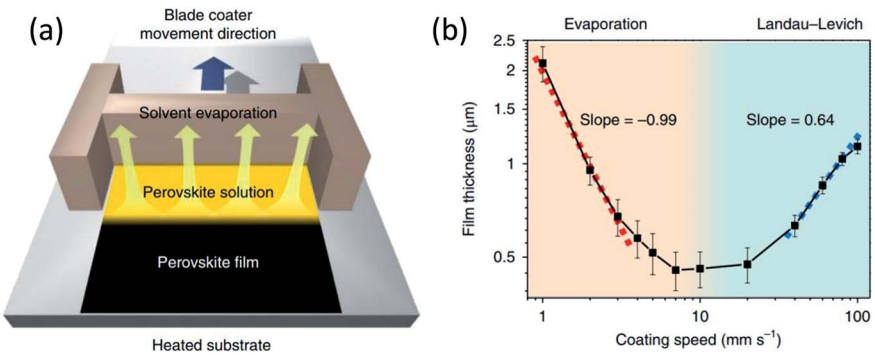

Fig. 9 (a) Schematic illustration of the hot-blade coating of a perovskite film. (b) Perovskite film's thickness as a function of coating speed by coating a 1 M $MAPbI_3$/DMF solution on a substrate preheated at 145 °C. Reproduced with permission from (ref. 49). Copyright 2018, Nature Publishing Group.

pyrrolidone (NCP) as the mediator in the precursor solution. They have demonstrated that the preformed uniform intermediate phase effected by the bar coating process enabled the formation of highly uniform perovskite films with a large area of 10×10 cm^2. PSCs fabricated by the wire-bar coating method using the resultant NCP-modified perovskite precursor solution exhibit superior photovoltaic performance with narrow distribution, as well as a smaller PCE loss in a larger active area than those obtained by using the spin-coating process. D. Jeong *et al.*[153] reported a coating solution suitable for large-area perovskite films fabricated by the wire-bar coating process. The coating solutions prepared by gas-mediated solid–liquid conversion already contain preformed perovskite clusters. $MAPbI_3$ films formed by wire-bar coating on a large area (>100 cm^2) exhibit tetragonal/cubic super-lattice structure with highly preferred orientation in the entire film, yielding average PCE of 17.01%.

4.1.1.3 Slot-die coating. The slot-die coating process (Fig. 8a) involves the transportation of the coating ink from the coating head to the substrate. Similar to the blade coating and wire-bar coating processes, a continuous meniscus is formed in the gap between the substrate and coating head. In principle, it is almost identical to the blade-coating or wire-bar coating processes. Similarly, the quality of the final solid perovskite film fabricated by slot-die coating strongly depends on the external strategies, which can control the nucleation and growth processes during the solidification process. Watson *et al.*[154] studied the effect of substrate temperature and air-knife blowing during slot-die coating on the formation of the perovskite film. On the basis of their results, they claimed that preheating the substrate to 65 °C with air-knife blowing could accelerate the drying kinetics and promote crystal growth. As a result, a wet film of the perovskite precursor could be rapidly dried, yielding a drastically increased precursor concentration, which, in turn, led to heterogeneous nucleation over the top surface of the warm substrate. Moreover, chemical additives have been applied in the perovskite precursor, broadening the processing window time and increasing the degree of crystallinity for perovskite films. For instance, Gao *et al.*[155] reported that the addition of NH_4Cl into $MAPbI_3$ perovskite precursor solution could lead to the formation of compact and uniform perovskite grains with high crystallinity. They suggested that the intermediate phases resulting from the introduction of NH_4^+ and Cl^- ions were proposed to increase the crystallinity of the final perovskite film. $MAPbI_3$ solar cells with 10 mg mL^{-1} NH_4Cl additive yielded 15.57% efficiency.

In contrast to blade or wire-bar coating processes, the ink flow can be better controlled in slot-die coating. However, slot-die coating typically requires a much higher amount of solution ink to fill the ink reservoir as well as the supply pipes and therefore is less suitable for laboratory applications or use in the optimization of new ink chemistries. As a consequence, slot-die coating has been less explored in research labs, and the corresponding PSCs have much lower PCE than their counterparts obtained by blade coating or wire-bar coating. On the other hand, when the materials cost is not a concern, such as that in company/manufacturing pilot lines, slot-die coating is indeed attractive for the uniform coating of thin films.

4.1.2 Spray coating. In the spray coating process, a nozzle is used to disperse tiny liquid droplets onto the substrates, as shown in Fig. 8b. Spray coating can be categorized according to the approach used for generating the droplets: electrospraying (*via* electrical repulsion), ultrasonic spraying (*via* ultrasonic vibration), or pneumatic spraying (*via* fast gas blowing). In earlier studies, ultrasonic spraying and pneumatic spraying have been frequently used for interlay deposition (compact oxide layer) in PSCs. Ultrasonic spraying methods have also been applied for perovskite photoactive layer deposition.[156–158] During the spray coating process, the size of the droplets and location of each droplet are random, and several droplets need to overlap in a local area to ensure complete coverage on the substrate. New droplets can dissolve the already deposited ones, which increases the processing complexity. In relation to this, heating the substrates at an elevated temperature can accelerate the evaporation rate of the solvent molecules and significantly alleviate the redissolution problem of the deposited material during the spray coating process.

Efforts have been made to balance the evaporation of solvent molecules and the redissolution problem by controlling the substrate temperature and engineering the ink solvent (mixing solvent and solvent additives, *etc.*).[157] In the electrospray coating method, a high voltage is applied between the spray nozzle and substrate. The droplets become smaller due to electrical repulsion, and the electric field increases the impact velocity of the droplets and the extent to which the droplets spread on the substrates.[159]

The quality of the perovskite film fabricated by spray coating depends on several factors, such as engineering the precursor solution (*e.g.*, the volatility of solvent molecules, designed amount of perovskite precursor solution, composition and ratio of lead halide and organic components, and so on), temperature of the substrates, and processing parameters (such as droplet size and spray speed). Although studies on mixed cation perovskites have extensively employed the spin-coating method,[41,42,160] spray coating has also been employed as a scalable fabrication process. For instance, $FA_{1-x}Cs_xPbI_3$ mixed cation films were prepared by a spray-assisted solution process.[127] Solar cell devices based on this mixed cation film showed enhanced stability and performance when compared with those based on $FAPbI_3$. The efficiency increased from 11.3% (for $FAPbI_3$) to 14.2% (for $FA_{0.9}Cs_{0.1}PbI_3$). After aging for 100 h under a relative humidity (RH) of 50%, the performance of $FA_{0.9}Cs_{0.1}PbI_3$-based devices remained constant at about 12.5%.

4.1.3 Inkjet printing. In the inkjet printing equipment configuration, miniaturized nozzles are applied to disperse the precursor ink from a piezoelectric-driven inkjet head, effecting better control over the droplet size and trajectory (Fig. 8c). Meanwhile, a shorter distance between the nozzles and substrate can yield an ultrafine lateral resolution, as demonstrated in digital printers. This patterning ability of inkjet printing is suitable for printed electronics.

Wei *et al.*[161] demonstrated inkjet printing for fabricating PSCs with a conventional structure by using the two-step deposition method employing a spin-coated PbI_2 layer followed by inkjet-printed MAI/carbon ink. They claimed that the consequent PSCs based on the mixed MAI/carbon ink exhibited significantly suppressed charge recombination, which can be ascribed to the improved interfacial contact between the perovskite light-harvesting layer and carbon layer. A PCE value of 11.60% was achieved for inkjet-printed PSCs. Li *et al.*[162] studied the influence of the temperature of printing table and MACl additive into the perovskite precursor solution on the perovskite film formation as well as the photovoltaic performance of the consequent PSCs. Mathies *et al.*[163] applied vacuum annealing after the inkjet-printing process, with the aim of optimizing the printing condition including the distance between the printed drops and the optimal number of printed sublayers. They indicated that the vacuum annealing process can lead to improved crystallinity, as well as compact and smooth perovskite film morphology. With regard to vacuum-annealed PSCs, efficiency of 11.3% has been obtained. Moreover, the printing speed is another factor that can influence inkjet printing for the large-area production of PSCs. Until now, the performance of spray-coated PSCs still lags behind their counterparts obtained using other scalable fabrication methods and therefore more efforts need to be expended toward exploring and optimizing the PSCs fabricated by the spray-coating methods.

4.1.4 Screen printing. Screen printing is a coating technique that has been widely applied to coat photoanodes in DSSCs.[164,165] In the screen-printing process (Fig. 8d, roll-to-roll version), a patterned-mesh screen is used to hold and transfer ink to the substrate. The open holes in the mesh can hold the viscous ink as a squeegee spreads the ink across the screen; this ink is then transferred onto the substrate to form the desired pattern, and the unwanted area of the mesh screen is blocked by the exposed photosensitive polymer emulsion. This method has good patterning ability with a lateral resolution of ~100 μm.[166] Generally, the thickness of the resultant solid film is determined by the thickness of the emulsion layer and size of the mesh. Screen printing has also been reported in the fabrication of PSCs.[167,168] The layer-by-layer printing process reported by Han *et al.* begins with the screen printing of TiO_2, followed by the printing of ZrO_2 and carbon electrodes. Then, a perovskite solution is dropped onto the mesoporous carbon electrode such that it infiltrates into mesoporous TiO_2 and ZrO_2. The printed ZrO_2 functions as a porous insulating layer to avoid direct contact between the TiO_2/FTO substrate and carbon electrode. The entire process can be viewed as a smartly designed variation of the mesoporous n–i–p structure, with distinct advantages in fabrication. Although screen printing is compatible for the scalable fabrication of PSCs, the infiltration of a perovskite precursor solution still remains a challenge. On the other hand, the technique shows lower efficiency as compared to those of the devices fabricated by other scalable approaches. The high stability and excellent outdoor performance of carbon-coated printed regular mesoporous PSCs has attracted research interest. Certified PCE of 12.8% and stable performance for over 1000 h in ambient air under full sunlight has been recorded for a device with an active area of 0.28 cm^2.[169] Perovskite solar cell modules with active areas of 31 and 70 cm^2 have been fabricated with large-scale screen printing processes[170] with efficiencies of 10.46% and 10.74%, respectively. The performance was stable (greater than 95%) without encapsulation under ambient conditions.

4.2 Nucleation and crystal growth control in scalable fabrication methods

The morphology of the perovskite photoactive layer plays a critical role in determining the photovoltaic performance of the corresponding PSCs. Scaling-up of PSCs requires scalable coating approaches that can uniformly deposit high-quality perovskite thin films over large-area substrates. Meanwhile, external strategies are required to control the nucleation and growth, as discussed in Chapter 2, to obtain a compact and highly crystalline perovskite thin film without pinholes and other defects. For the natural slow-drying process of the wet film with a perovskite precursor ($MAPbI_3$), the perovskite nuclei are prone to adopting preferential growth and form thin films with dendritic structures,[171] leading to inadequate surface coverage on the substrates and consequently yield solar cells with low PCE. This has stressed the importance of nucleation and growth control during the solution-state to solid-state transformation by the use of external strategies. External strategies applied to control nucleation and crystal growth in order to influence the perovskite film formation mechanism can be categorized into two approaches: physical approaches and chemical approaches. Tuning the drying kinetics during the solution-to-solid phase transition is the primary means for physical approaches to control the growth process of perovskite thin films. For chemical approaches, chemical additives are used to control the crystal growth. Based on these strategies, compact and smooth perovskite thin films can be obtained by scalable fabrication methods over a large area, subsequently yielding large-sized PSCs.

4.2.1 Physical approaches to control perovskite film formation. Physical approaches are usually applied to control the drying kinetics by tuning the volatility of solvent molecules. The accelerated removal rate of the solvent molecules from perovskite precursor solutions results in an increased degree of supersaturation, leading to higher nucleation density and shorter grain growth times. Coupled with a higher nucleation density, a shorter growth time significantly suppresses the overgrowth of any individual nuclei to form large dendritic structures. The accelerated removal of solvent molecules can be achieved by antisolvent extraction,[21,172,173] heating,[31–33] gas blowing,[26–28] vacuum treatment,[36,37] or a combination of these physical approaches,[174] as shown in Fig. 10.

4.2.1.1 Antisolvent engineering. The antisolvent approach was first introduced by Seok *et al.*[21] in 2014; since then, it has been widely applied to obtain smooth and compact perovskite thin films. The so-called antisolvents need to be miscible with the solvents used to dissolve the perovskite precursors, and the perovskite itself should not be soluble in the antisolvent.

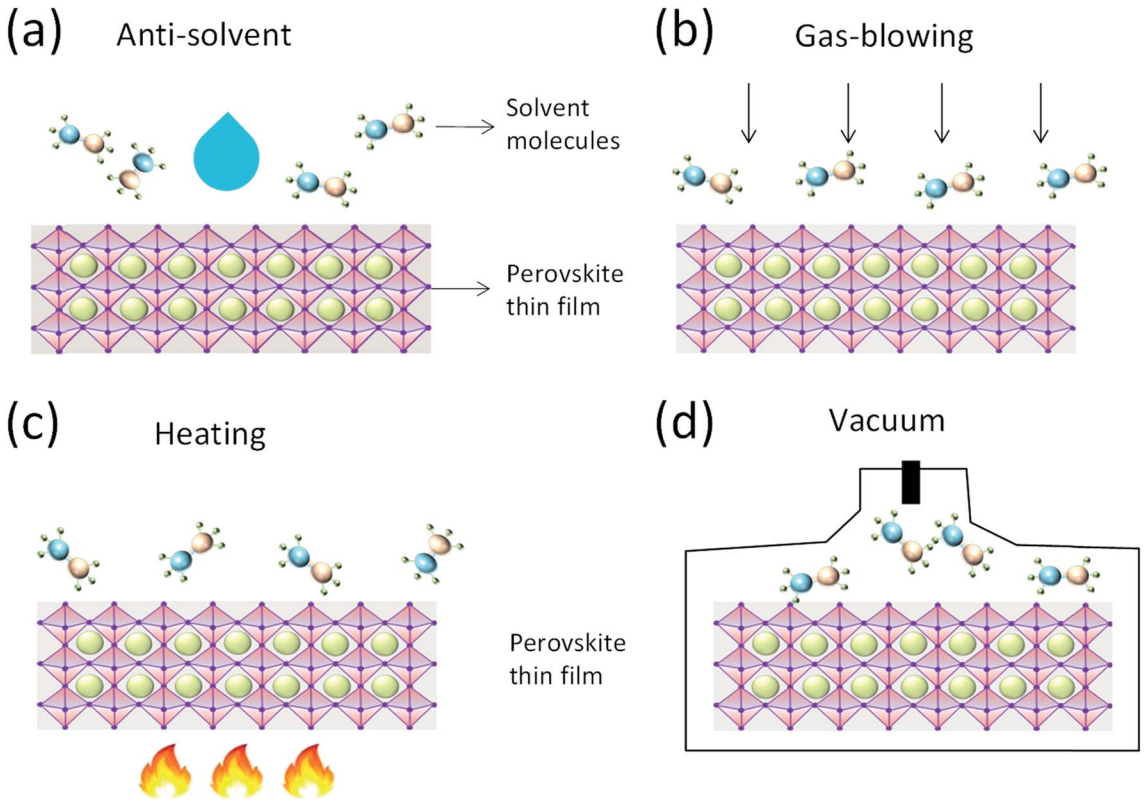

Fig. 10 Physical approaches to increase the degree of supersaturation by (a) antisolvent engineering, (b) gas blowing, (c) heating effect, and (d) vacuum treatment for an accelerated evaporation rate of solvent molecules.

Antisolvents induce the fast extraction of solvent molecules from the precursor solutions and therefore can lead to the rapid supersaturation of the perovskite precursor film and fast nucleation of the perovskite film. Diverse antisolvents have been reported in the fabrication of PSCs, such as toluene,[175] chlorobenzene,[21] hexane,[176] ethylacetate,[177] anisole,[178] ethyl ether,[179] and mixed ones.[180] Antisolvent dripping combined with spin-coating deposition has been widely used in the laboratory fabrication of top-performing PSCs. As compared to the antisolvent dripping method used during the spin-coating process, more uniform perovskite films can be obtained by the spraying of an antisolvent.[181] Furthermore, the spraying process of the antisolvent can be compatible with large-sized perovskite solar cell fabrication in contrast to antisolvent dripping, and a PCE value of 12.1% for PSCs with a large area (16 cm^2) has also been reported.[182] Aiming to apply the antisolvent strategy into scalable deposition approaches, the antisolvent bathing method has also been developed, namely, the perovskite precursor film is soaked in an antisolvent bath for a certain period of time.[179] These are the main progresses made in the application of antisolvents in large-area PSCs.

4.2.1.2 Heat/temperature effect. In solution-processed perovskite thin films, the formation of the solid perovskite film is a transition from the solution state to the solid state with the evaporation of the solvent molecules, which emphasizes the importance of drying kinetics or removal rate of solvent molecules. Heating is another physical approach that can accelerate the evaporation rate of the solvent molecules during the solution-to-solid phase transition, influencing the degree of supersaturation and consequently perovskite nucleation and growth (according to the LaMer theory discussed in Chapter 2). A hot-casting technique has been used to deposit perovskite thin films.[34] Here, the perovskite precursor solution or the substrates were heated to an elevated temperature, rapidly evaporating the solvent molecules to. As compared to other strategies, heating the perovskite precursor ink or substrate during deposition is relatively easier, which enabled this heating approach to be widely used to control the perovskite film morphology in different scalable coating methods, including spray coating,[183] dip coating,[184] blade coating,[51] slot-die coating,[185] *etc.*

For the hot-blade coating process,[186–188] the elevated temperature could not only accelerate the evaporation rate of the solvent molecules, but also stimulate the solute atoms more easily to overcome the diffusion energy barrier and therefore lead to faster grain growth with a larger domain size. Upon using this approach, decent PCE (up to 20.3%)[49] has been obtained.

4.2.1.3 Gas blowing. Another simple yet effective physical approach is gas blowing (Fig. 11), which can be used to control the drying kinetics and has also been used to fabricate a smooth perovskite film for use in PSCs. Furthermore, this physical approach is compatible with different scalable fabrication approaches for fabricating perovskite thin films. During the

gas-blowing process, an inert gas (*e.g.*, N_2) is typically used in the investigation. The applied gas blowing mainly expedites the evaporation rate of the solvent molecules and increases the degree of supersaturation, effecting control over perovskite nucleation and growth. Therefore, the blowing rate strongly influences the morphology of the final perovskite thin film, which has been systematically explored in earlier studies.[26–28] A smooth (surface root-mean-square (RMS) roughness of 4.98 nm as characterized by AFM within a scan area of 10×10 mm^2) and compact perovskite film was obtained by gas blowing at room temperature under ambient conditions.[48]

4.2.1.4 Vacuum treatment. Vacuum treatment has also been applied to facilitate the evaporation rate of solvent molecules during the transition from the perovskite precursor solution to solid film. Parvazian *et al.*[189] reported the vacuum-assisted meniscus printing method, where a photoactive perovskite film with optimal performance was achieved. In this fabrication approach, a vacuum chamber (<100 Pa) was used for 30 s to actively remove the solvent molecules at an appropriate pace from the as-coated wet perovskite precursor films. After using this vacuum process, in contrast to low surface coverage, needle-like morphology from the natural slow-drying, pinhole-free, smooth, and compact film with appropriate grain-size perovskite thin film was obtained. The perovskite devices with the resultant perovskite-absorbing layer yield PCE of 10.1% (active area: 0.1 cm^2). Furthermore, efficiency of 8.0% was achieved for an active area of 1 cm^2. In addition, a vacuum flash drying method has also been reported to extract the solvent. With this technique, large-area PSCs (>1 cm^2) with PCE values >20% could be achieved.[190] With further development, an apparatus has been designed to simultaneously apply a low pressure and strong gas blowing over the wet film on the substrate; the combined influence of the vacuum and gas blowing increased the solvent removal rate.[174]

4.2.2 Chemical approaches to control perovskite film formation. Besides the drying kinetics affected by the physical approaches, nucleation and crystal growth were also significantly influenced by the chemistry of the perovskite precursors, including varying the chemical composition of the perovskite or introducing additives into the precursor solution. It has been widely reported that the addition of a marginal amount of chemical additive in the perovskite precursor solution could be an effective and reliable strategy to control the crystallization process, including the perovskite thin-film morphology, perovskite grain size, and consequently the PCE of the PSC devices. For instance, it has been reported that perovskite thin films formed by the perovskite precursor solution such as chloride ions ($PbCl_2$ + 3 MAI) showed better coverage and had a larger grain size than those obtained from a stoichiometric precursor (PbI_2 + MAI).[40] Additional chloride additives have been

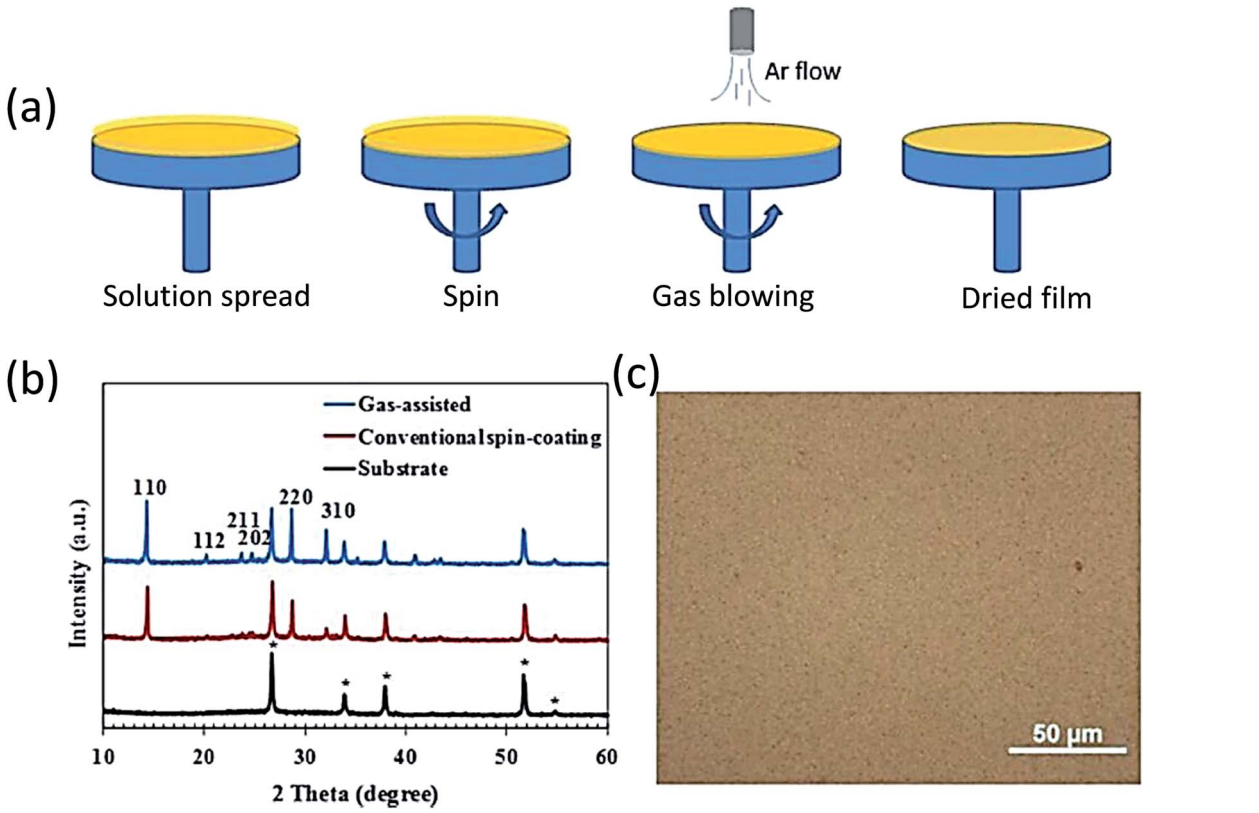

Fig. 11 (a) Schematic diagram showing the procedure for gas-assisted spin-coating method; (b) XRD patterns of the FTO/glass substrate and perovskite films made by the gas-assisted method as well as the conventional spin-coating method (diffraction peaks for the FTO crystal are marked by *); (c) an optical microscope image of the perovskite film fabricated by the gas-assisted method. The films were annealed at 100 °C for 10 min. Reproduced with permission from (ref. 171). Copyright 2014, Elsevier Inc.

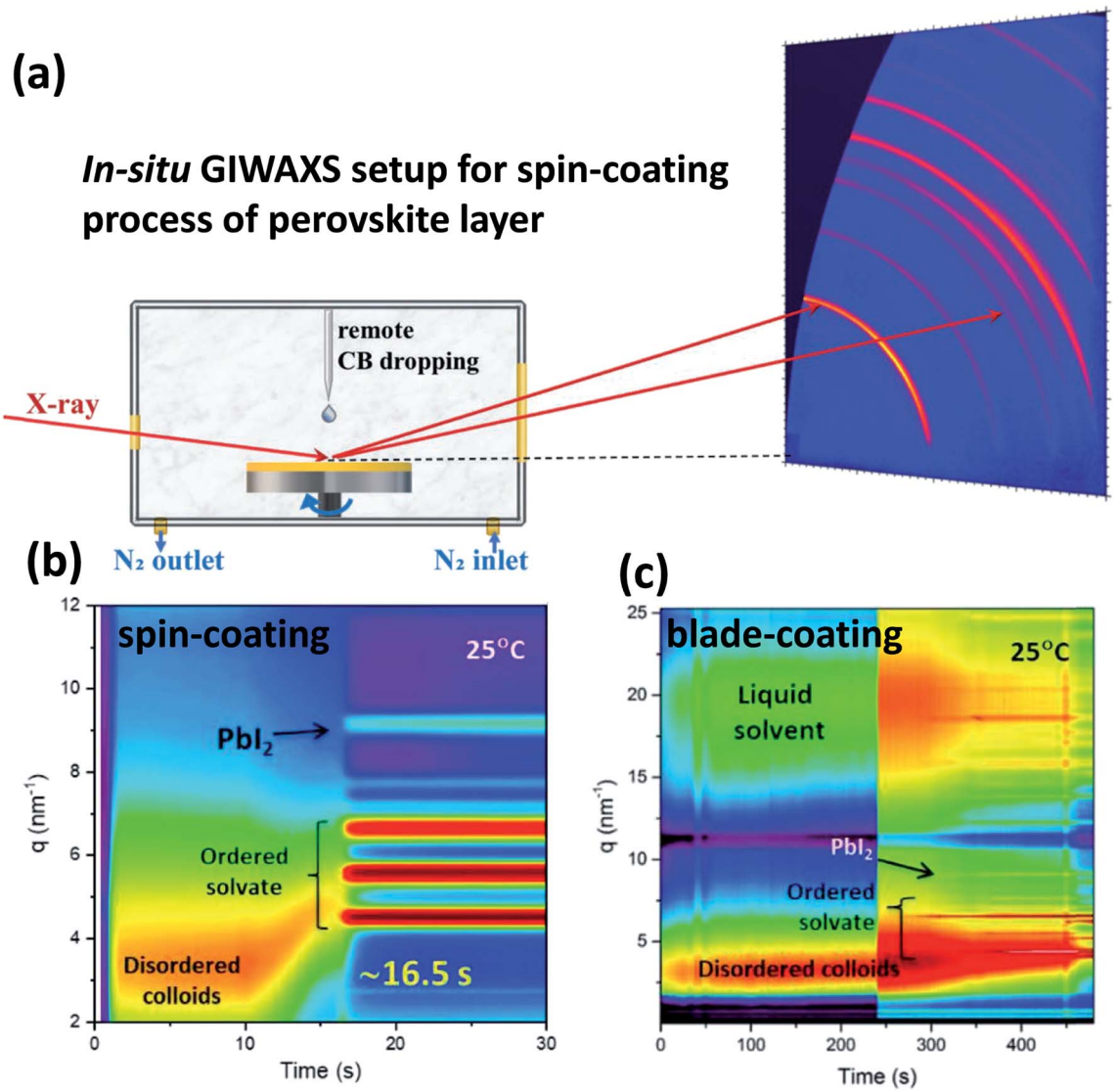

Fig. 12 (a) Schematic of *in situ* GIWAXS setup for the spin-coating process in order to explore the mixed-perovskite crystallization mechanism.[209] A comparison of the *in situ* GIWAXS carried out during (b) spin coating and (c) blade coating of hybrid perovskite films at room temperature.[210]

reportedly used as additives in perovskite precursor solutions, yielding perovskite thin films with similar morphologies as those obtained with $PbCl_2$.[191–193] With regard to the chemistry aspect, it is believed that Cl^- can compete with I^- to coordinate to Pb^{2+}, which significantly suppresses the formation of Pb–I–Pb in addition to the nuclei in the perovskite precursor solution.[84] The chloride ions in the perovskite precursor solution can slow down the nucleation and crystal growth, but they also induce the formation of chloride-containing intermediate phases in the perovskite precursor solid film when the solvent molecules are volatized. Although it yields a less crystalline perovskite thin film than that obtained from a stoichiometric precursor (PbI_2 + MAI), a smooth and compact perovskite thin film can be obtained rather than one with poor coverage (morphology including dendrites or pinholes).[194,195] In addition to chloride-containing additives, lead(II) acetate and other organic halides have been reported for use as additives in a precursor solution for obtaining uniform perovskite morphology by forming intermediate phases.[38,39] Moreover, hydrohalic acids (HCl, HBr, or HI) have also been used as additives in the perovskite precursor solution in order to fabricate compact and smooth perovskite thin films.[196,197] There are two mechanisms affecting the perovskite film growth based on hydrohalic acids: first, more anions are provided by the added hydrohalic acids to coordinate to the lead ions, yielding the formation of an intermediate film after the removal of the solvent molecules and consequently slowing down the perovskite nucleation process;[198] second, the added hydrohalic acids can lower the pH value of the perovskite precursor solution, breaking down smaller clusters or nuclei, significantly suppressing the nucleation and crystal growth of the individual domains.[199] The common perovskite precursor solvents are polar aprotic solvents (*e.g.*, DMF and DMSO), which contain strong electronegative polar groups with C=O or S=O. These

Lewis base polar solvents can react with PbI_2 (Lewis acid property) and form a stable intermediate phase such as PbI_2–DMSO or MAI–PbI_2–DMSO. The O/N in the active carbonyl, acyl, and cyano groups in the solvent molecules are the key to react with Pb. Based on this strategy, functional additives with carbonyl, acyl, and cyano groups with lone pairs of electrons in the molecules have also been adopted, which react with PbI_2. Similarly, retarding crystallization and high-quality perovskite film formation have also been reported. For example, Choy *et al.*[200] added high-boiling-point additives, *i.e.*, 4-*tert*-butylpyridine (TBP), into the PbI_2 precursor solution to form complexes with PbI_2 for the complete conversion into perovskites. TBP is utilized as a nitrogen donor ligand to form a coordination complex ($PbI_2 \cdot x$TBP). Assisted by the removal of the thermal solvent, this forms a porous and uniform PbI_2 film, which facilitates the permeation of MAI and induces fast crystallization to yield smooth perovskite film morphology. A TBP additive can also be added into the MAI solution to achieve a $MAPbI_3$ film with larger grains and high crystallinity, again due to the reaction between TBP and PbI_2. Jen *et al.*[201] added 1,8-diiodooctane (DIO) into the perovskite precursor and achieved a uniform and dense perovskite layer. The DIO–Pb^{2+} chelation was proposed to improve the solubility of PbI_2, promote the homogeneous nucleation of perovskite, and regulate the crystallization rate of perovskite. Methylammonium formate (MAF) has been widely applied to assist in perovskite film growth. MAF has the C=O bond in the acetate anion, which can form a Pb–COOH complex, followed by replacement by I^- during the annealing process. The process slows down the perovskite crystal growth and therefore leads to a dense perovskite film with a larger grain size.[202] The sulfonate group with oxygen is also shown to be able to slow down the MAI–PbI_2 reaction, leading to the formation of a uniform high-quality perovskite film. Zhou *et al.*[203] studied the 4-(1*H*-imidazol-3-ium-3-yl) butane-1-sulfonate (IMS) additive and showed that the oxygen atom on the sulfonate group with a lone electron pair within the molecule could function as a coordination ligand with Pb^{2+} ions, leading to the formation of a $MAPbI_3$–IMS intermediate. Pyrrole (Pr) has also been examined as an additive into the perovskite precursor as the N atom in the Pr ring induces the Lewis base property and therefore can form a complex with Pb ions.[204] In addition, Pr can form hydrogen bonds with organic cations. Huang *et al.*[205,206] systemically studied the effect of methylammonium acetate (MAAc) on the perovskite film formation mechanism. They suggested that MAAc can facilitate the formation of a uniform perovskite film with controlled surface morphology by retarding the reaction between PbI_2 and MAI in the solution. The formation process of $MAPbI_3$ was allowed *via* the exchange of I^- from the adjacent MAI molecules and Ac^- from the intermediate phases, yielding the maximum PCE of 18.09%.[205] In addition, they demonstrated that MAAc can be applied as a novel solvent in the fabrication of PSCs under ambient conditions with a nonhazardous characteristic. It yields a pinhole-free dense perovskite film upon a simple one-step method with no need for an antisolvent even under a higher relative humidity (>80%). Under optimized processing conditions, an average PCE value of 18.42% and maximum efficiency of 20.05% were obtained with improved stability.[206] Furthermore, surfactants (such as L-α-phosphatidylcholine) have also been applied in the perovskite film formation process in scalable fabrication processes. Huang's group suggested that the addition of very small amounts of L-α-phosphatidylcholine can remarkably alter the fluid drying dynamics and enhance the adhesion of the perovskite precursor solution onto the underlying layer. This enables the blading of a smooth perovskite film at a high coating speed with RMS roughness of 14.5 nm. Meanwhile, it can also passivate charge traps, yielding a PCE value of over 20% for small-area PSCs and PCE of 15.3% for perovskite modules (33.0 cm^2).[49]

In addition, the Lewis acid–base theory was also applied in perovskite film growth. Based on this theory, electron donors and acceptors were defined as Lewis bases and Lewis acids, respectively. Lead(II) halides are strong Lewis acids, which can readily form adducts with Lewis base materials, including additives or solvents. The resultant Lewis acid–base adducts in the precursor solution can increase the solubility of lead halides, slowing the nucleation and crystal growth process. By tuning the interaction degree between Lewis acids and Lewis bases by choosing different Lewis base materials, the nucleation and growth rate can be controlled, eventually improving the morphology of the final perovskite thin film.[201,207,208]

4.3 Stability of massive fabricated perovskite modules

The stability of perovskite photovoltaic modules plays a crucial role in ensuring the deployment of perovskite photovoltaic technology. Upon a better understanding of the degradation mechanisms of PSCs, significant progress has been achieved in terms of improving the stability of PSCs at the laboratory scale due to the intensive worldwide research effort. In particular, the issue of PSC stability has been reviewed in detail elsewhere.[211,212] In short, the combination of tuning the perovskite composition, choosing of interlayer materials and electrode materials, device structure, and interface engineering forms an integrated comprehensive approach to improve the stability of PSCs.

It is noteworthy that the degradation mechanism at the perovskite module level becomes much more complex than that at the laboratory-scale single-cell level. First, the production of perovskite modules requires more complicated processing and is preferable to be conducted in the ambient air environment (humidity-controlled cleanroom rather than an inert gas environment), leading to the degradation of perovskite modules induced by ambient fabrication and additional processing procedures. For perovskite modules based on monolithic interconnection, the interconnection degradation can also be induced by the partial shading or structure failure due to ion migration; while for partially shaded modules, there is high reverse bias applied on the shaded cells. This can lead to local hotspots as well as inverted-bias junction damage[213,214] in the perovskite module configuration. Bypass diodes have been used to resolve the shading problem in current photovoltaic technology, but building these diodes in each sub-cell in a monolithic module is difficult. These external factors can also

facilitate the degradation of perovskite modules in comparison to single laboratory-scale PSCs.

5. Conclusions and perspective

Because of the dramatic improvements in the photovoltaic performance of organic–inorganic hybrid PSCs, scaling-up the perovskite photovoltaic technology has become increasingly attractive worldwide as a research topic. Until now, overcoming the different challenges involved in the massive manufacturing process is still in its infancy, such as device architecture, material deposition approaches, photovoltaic performance, stability, and efficient schemes for module interconnection.

Besides the scaling-up issue for massive manufacturing discussed in this review, long-term stability is another serious issue that can hinder the application value. Consequently, intensive efforts have been directed toward improving the stability of PSCs with excellent progress. Recently, Wang *et al.*[215] reported that the europium ion pair (Eu^{3+}–Eu^{2+}) can act as the "redox shuttle" that can selectively and simultaneously oxidize Pb^0 and reduce I^0 defects in a cyclical transition. As a result, a perovskite device could achieve certified PCE of 20.52% with significantly improved long-term durability. Huang *et al.*[216] converted lead halide perovskite surfaces into water-insoluble lead(II) oxysalts *via* reactions with phosphate or sulfate ions, which can effectively stabilize the perovskite surface and bulk material. Furthermore, the capping lead oxysalt layers can also reduce the defect density on the perovskite surfaces by passivating undercoordinated surface lead centers (defect-nucleating sites), yielding improved photovoltaic performance. Karunadasa *et al.*[217] demonstrated layered perovskites, namely, $(PEA)_2(MA)_2(Pb_3I_{10})$, with significantly improved stability against moisture (RH: 52%) for more than 40 days due to the intrinsic hydrophobic property of the long organic cations. Since then, investigations involving 2D or reduced-dimensional PSCs has attracted significant attention due to the remarkably improved stability under ambient conditions. Due to the scarified PCE of 2D perovskite structures, mixed 2D/3D perovskites[218,219]and graded 2D/3D perovskites[220,221] have been designed with enhanced stability and respectable PCE. Moreover, encouraged by the thermal stability property, remarkable progress has been achieved in all-inorganic PSCs with PCE of $CsPbI_3$ exceeding 16%.[222] Quite recently, Zhao *et al.*[223] synthesized the β-phase (tetragonal) of $CsPbI_3$ from CsI and $HPbI_3$. The passivation of the surface trap state has boosted PCEs up to 18%. Meanwhile, the kinetics and formation mechanism of the perovskite phase has been emphasized by recent research.[224,225] *In situ* grazing-incidence wide-angle X-ray scattering (GIWAXS) is a powerful tool to study the formation mechanism during the process of coating, offering a key insight into controlling the quality of a perovskite film.[209]

Scaling-up is one of the most urgent challenges needed to be addressed for perovskite solar cell technology toward large-area devices involving massive manufacturing. This review has tried to cover the comprehensive recent studies ranging from classical nucleation and crystal growth to scalable solution deposition approaches beyond the non-scalable spin-coating method. Further to the classical nucleation and growth processes as summarized in the initial chapter, common PSC architectures and recent progresses made in the deposition methods of perovskite materials have been discussed. Although both electrodeposition and vapor-phase deposition have the potential to be applied for the deposition of perovskite thin films over large areas, both these methods often require more complicated procedures and more sophisticated equipment, hindering their applications for the low-cost fabrication promise of PSCs. In contrast, solution-processed perovskite thin films not only yield outstanding photovoltaic performance but also are much more compatible with low-cost scalable manufacturing. It has been intensively emphasized that perovskite film morphology plays a key role in determining the photovoltaic performance of PSCs. Classical nucleation, including homogeneous nucleation, heterogeneous nucleation, and crystal growth mechanisms pertaining to the surface reaction and monomer diffusion onto the surface, has been systematically summarized in this review. It has been demonstrated that perovskite crystal growth can be controlled by the monomer diffusion process, as per Fick's first law. This prerequisite enables the LaMer model to be applied in solution-processed perovskite films and consequently has been widely used to explain the morphological differences in perovskites based on nucleation and crystal growth understandings. Scalable solution-processed coating techniques such as meniscus coating (*e.g.*, blade coating, wire-bar coating, slot-die coating, *etc.*), spray coating, inkjet printing, and screen printing have been applied in the deposition of perovskite photoactive layers, as described in this review. Based on the in-depth understanding of perovskite nucleation and crystal growth, strategies applied during the fabrication process to control perovskite film formation have been summarized and categorized into physical approaches and chemical approaches; they have been comprehensively investigated in this work. Although promising results are obtained for the scalable fabrication of PSCs, different challenges still persist. Even for laboratory-scale PSCs, decent photovoltaic performance and/or enhanced stability have been reported from diverse combinations of device architectures, materials, as well as the complex composition of perovskite light-harvesting layers, without reliable recipes that are highly reproducible. Additional efforts will be needed for perovskite photovoltaic technology so that it can be transferred to massive manufacturing (modules) due to the different processing properties. Maintaining the high light-to-electricity efficiency with long-term stability under operation conditions, minimizing the negative influence of the environment, and lowering the fabrication cost are the main challenges for large-scale module fabrication in the near future. Methods such as high-temperature blading and understanding the perovskite film formation mechanism still need to be improved with more powerful tools. *In situ* study tools (particularly *in situ* GIWAXS, *etc.*) can help to provide critical insightful information in the understanding of the perovskite crystal/film formation. For instance, for the prototypical high-performance mixed-perovskite composition, *i.e.*, $Cs_x(FA_{0.83}MA_{0.17})_{1-x}Pb(I_{0.83}Br_{0.17})_3$, Lu's group comprehensively investigated the

crystallization process, as well as the role of Cs^+ ions in altering the phase-transition process (Fig. 12a). For a better understanding of perovskite film formation, three phase-formation steps have been identified with the help of *in situ* GIWAXS: (I) perovskite precursor solution; (II) hexagonal δ-phase; (III) complex phases such as MAI–PbI_2–DMSO intermediate phases, hexagonal polytypes, and perovskite α-phase. To transfer the spin-coating process to the blade-coating process, synchrotron-based *in situ* GIWAXS was used for undertaking the different crystallization processes for these two methods (Fig. 12b and c), yielding useful insights into the optimization of blade-coated PSCs.

We hope that this review can prove to be a useful guide to understand the intrinsic and natural phenomena pertaining to perovskite nucleation and growth processes from the viewpoint of perovskite precursor solution engineering, highlighting the recent progresses made in perovskite film formation control in scalable fabrication methods; this can stimulate more advanced studies in this promising field.

Conflicts of interest

There are no conflicts to declare.

Acknowledgements

G. L. thanks the Research Grants Council of Hong Kong (GRF grants 15246816 and 15218517), the Project of Strategic Importance provided by the Hong Kong Polytechnic University (Project Code: 1-ZE29), and Shenzhen Science and Technology Innovation Commission (Project No. JCYJ20170413154602102). The financial support from the National Natural Science Foundation of China (21875144) and (51778369) is gratefully acknowledged.

References

1 National Renewable Energy Laboratory solar cell efficiency chart, http://www.nrel.gov/pv/assets/images/efficiency-chart.png.
2 A. R. b. M. Yusoff and M. K. Nazeeruddin, *J. Phys. Chem. Lett.*, 2016, **7**, 851–866.
3 L. Etgar, *Energy Environ. Sci.*, 2018, **11**, 234–242.
4 A. M. A. Leguy, P. Azarhoosh, M. I. Alonso, M. Campoy-Quiles, O. J. Weber, J. Yao, D. Bryant, M. T. Weller, J. Nelson, A. Walsh, M. van Schilfgaarde and P. R. F. Barnes, *Nanoscale*, 2016, **8**, 6317–6327.
5 A. Ng, Z. Ren, H. Hu, P. W. K. Fong, Q. Shen, S. H. Cheung, P. Qin, J.-W. Lee, A. B. Djurišić, S. K. So, G. Li, Y. Yang and C. Surya, *Adv. Mater.*, 2018, **30**, 1804402.
6 P.-L. Qin, G. Yang, Z. Ren, S. H. Cheung, S. K. So, L. Chen, J. Hao, J. Hou and G. Li, *Adv. Mater.*, 2018, **30**, 1706126.
7 S. A. Kulkarni, T. Baikie, P. P. Boix, N. Yantara, N. Mathews and S. Mhaisalkar, *J. Mater. Chem. A*, 2014, **2**, 9221–9225.
8 M. Ye, X. Hong, F. Zhang and X. Liu, *J. Mater. Chem. A*, 2016, **4**, 6755–6771.
9 H. Hasegawa, K. Kobayashi, Y. Takahashi, J. Harada and T. Inabe, *J. Mater. Chem. C*, 2017, **5**, 4048–4052.
10 D. Meggiolaro, S. G. Motti, E. Mosconi, A. J. Barker, J. Ball, C. Andrea Riccardo Perini, F. Deschler, A. Petrozza and F. De Angelis, *Energy Environ. Sci.*, 2018, **11**, 702–713.
11 Z. Bi, X. Rodríguez-Martínez, C. Aranda, E. Pascual-San-José, A. R. Goñi, M. Campoy-Quiles, X. Xu and A. Guerrero, *J. Mater. Chem. A*, 2018, **6**, 19085–19093.
12 D. N. Dirin, L. Protesescu, D. Trummer, I. V. Kochetygov, S. Yakunin, F. Krumeich, N. P. Stadie and M. V. Kovalenko, *Nano Lett.*, 2016, **16**, 5866–5874.
13 F. Zhang, B. Yang, Y. Li, W. Deng and R. He, *J. Mater. Chem. C*, 2017, **5**, 8431–8435.
14 M. H. Du, *J. Mater. Chem. A*, 2014, **2**, 9091–9098.
15 L. Ma, F. Hao, C. C. Stoumpos, B. T. Phelan, M. R. Wasielewski and M. G. Kanatzidis, *J. Am. Chem. Soc.*, 2016, **138**, 14750–14755.
16 Z. Song, C. L. McElvany, A. B. Phillips, I. Celik, P. W. Krantz, S. C. Watthage, G. K. Liyanage, D. Apul and M. J. Heben, *Energy Environ. Sci.*, 2017, **10**, 1297–1305.
17 J. Zheng, C. F. J. Lau, H. Mehrvarz, F.-J. Ma, Y. Jiang, X. Deng, A. Soeriyadi, J. Kim, M. Zhang, L. Hu, X. Cui, D. S. Lee, J. Bing, Y. Cho, C. Chen, M. A. Green, S. Huang and A. W. Y. Ho-Baillie, *Energy Environ. Sci.*, 2018, **11**, 2432–2443.
18 G. Yang, P. Qin, G. Fang and G. Li, *J. Energy Chem.*, 2018, **27**, 962–970.
19 A. Kojima, K. Teshima, Y. Shirai and T. Miyasaka, *J. Am. Chem. Soc.*, 2009, **131**, 6050–6051.
20 H.-S. Kim, C.-R. Lee, J.-H. Im, K.-B. Lee, T. Moehl, A. Marchioro, S.-J. Moon, R. Humphry-Baker, J.-H. Yum, J. E. Moser, M. Grätzel and N.-G. Park, *Sci. Rep.*, 2012, **2**, 591.
21 N. J. Jeon, J. H. Noh, Y. C. Kim, W. S. Yang, S. Ryu and S. Il Seok, *Nat. Mater.*, 2014, **13**, 897–903.
22 H. Tan, A. Jain, O. Voznyy, X. Lan, F. P. García de Arquer, J. Z. Fan, R. Quintero-Bermudez, M. Yuan, B. Zhang, Y. Zhao, F. Fan, P. Li, L. N. Quan, Y. Zhao, Z.-H. Lu, Z. Yang, S. Hoogland and E. H. Sargent, *Science*, 2017, **355**, 722–726.
23 C. Wang, C. Xiao, Y. Yu, D. Zhao, R. A. Awni, C. R. Grice, K. Ghimire, I. Constantinou, W. Liao, A. J. Cimaroli, P. Liu, J. Chen, N. J. Podraza, C.-S. Jiang, M. M. Al-Jassim, X. Zhao and Y. Yan, *Adv. Energy Mater.*, 2017, **7**, 1700414.
24 D.-Y. Son, J.-W. Lee, Y. J. Choi, I.-H. Jang, S. Lee, P. J. Yoo, H. Shin, N. Ahn, M. Choi, D. Kim and N.-G. Park, *Nat. Energy*, 2016, **1**, 16081.
25 D. Bi, W. Tress, M. I. Dar, P. Gao, J. Luo, C. Renevier, K. Schenk, A. Abate, F. Giordano, J.-P. Correa Baena, J.-D. Decoppet, S. M. Zakeeruddin, M. K. Nazeeruddin, M. Gra tzel and A. Hagfeldt, *Sci. Adv.*, 2016, **2**, e1501170.
26 L.-L. Gao, C.-X. Li, C.-J. Li and G.-J. Yang, *J. Mater. Chem. A*, 2017, **5**, 1548–1557.
27 M. Zhang, H. Yu, J.-H. Yun, M. Lyu, Q. Wang and L. Wang, *Chem. Commun.*, 2015, **51**, 10038–10041.
28 K. Hwang, Y. S. Jung, Y. J. Heo, F. H. Scholes, S. E. Watkins, J. Subbiah, D. J. Jones, D. Y. Kim and D. Vak, *Adv. Mater.*, 2015, **27**, 1241–1247.

29 C.-H. Chiang and C.-G. Wu, *ACS Nano*, 2018, **12**, 10355–10364.
30 T. Gotanda, S. Mori, H. Oooka, H. Jung, H. Nakao, K. Todori and Y. Nakai, *J. Mater. Res.*, 2017, **32**, 2700–2706.
31 H.-C. Liao, P. Guo, C.-P. Hsu, M. Lin, B. Wang, L. Zeng, W. Huang, C. M. M. Soe, W.-F. Su, M. J. Bedzyk, M. R. Wasielewski, A. Facchetti, R. P. H. Chang, M. G. Kanatzidis and T. J. Marks, *Adv. Energy Mater.*, 2017, **7**, 1601660.
32 Z. Wang, X. Liu, Y. Lin, Y. Liao, Q. Wei, H. Chen, J. Qiu, Y. Chen and Y. Zheng, *J. Mater. Chem. A*, 2019, **7**, 2773–2779.
33 M. K. Kim, H. S. Lee, S. R. Pae, D.-J. Kim, J.-Y. Lee, I. Gereige, S. Park and B. Shin, *J. Mater. Chem. A*, 2018, **6**, 24911–24919.
34 W. Nie, H. Tsai, R. Asadpour, J.-C. Blancon, A. J. Neukirch, G. Gupta, J. J. Crochet, M. Chhowalla, S. Tretiak, M. A. Alam, H.-L. Wang and A. D. Mohite, *Science*, 2015, **347**, 522–525.
35 J. E. Bishop, J. A. Smith, C. Greenland, V. Kumar, N. Vaenas, O. S. Game, T. J. Routledge, M. Wong-Stringer, C. Rodenburg and D. G. Lidzey, *ACS Appl. Mater. Interfaces*, 2018, **10**, 39428–39434.
36 G. M. Kim and T. Tatsuma, *J. Phys. Chem. C*, 2016, **120**, 28933–28938.
37 F. X. Xie, D. Zhang, H. Su, X. Ren, K. S. Wong, M. Grätzel and W. C. H. Choy, *ACS Nano*, 2015, **9**, 639–646.
38 M. Yang, Y. Zhou, Y. Zeng, C.-S. Jiang, N. P. Padture and K. Zhu, *Adv. Mater.*, 2015, **27**, 6363–6370.
39 W. Zhang, M. Saliba, D. T. Moore, S. K. Pathak, M. T. Hörantner, T. Stergiopoulos, S. D. Stranks, G. E. Eperon, J. A. Alexander-Webber, A. Abate, A. Sadhanala, S. Yao, Y. Chen, R. H. Friend, L. A. Estroff, U. Wiesner and H. J. Snaith, *Nat. Commun.*, 2015, **6**, 6142.
40 M. M. Lee, J. Teuscher, T. Miyasaka, T. N. Murakami and H. J. Snaith, *Science*, 2012, **338**, 643–647.
41 M. Saliba, T. Matsui, J.-Y. Seo, K. Domanski, J.-P. Correa-Baena, M. K. Nazeeruddin, S. M. Zakeeruddin, W. Tress, A. Abate, A. Hagfeldt and M. Grätzel, *Energy Environ. Sci.*, 2016, **9**, 1989–1997.
42 D.-Y. Son, S.-G. Kim, J.-Y. Seo, S.-H. Lee, H. Shin, D. Lee and N.-G. Park, *J. Am. Chem. Soc.*, 2018, **140**, 1358–1364.
43 M. Salado, L. Calió, L. Contreras-Bernal, J. Idígoras, J. Anta, S. Ahmad and S. Kazim, *Materials*, 2018, **11**, 1073.
44 X. Jia, Z. Hu, J. Xu, L. Huang, J. Zhang, J. Zhang and Y. Zhu, *Appl. Phys. Lett.*, 2017, **111**, 243902.
45 Y. Li, L. Ji, R. Liu, C. Zhang, C. H. Mak, X. Zou, H.-H. Shen, S.-Y. Leu and H.-Y. Hsu, *J. Mater. Chem. A*, 2018, **6**, 12842–12875.
46 L. Zheng, D. Zhang, Y. Ma, Z. Lu, Z. Chen, S. Wang, L. Xiao and Q. Gong, *Dalton Trans.*, 2015, **44**, 10582–10593.
47 R. Wang, M. Mujahid, Y. Duan, Z.-K. Wang, J. Xue and Y. Yang, *Adv. Funct. Mater.*, 2019, 1808843.
48 H. Hu, Z. Ren, P. W. K. Fong, M. Qin, D. Liu, D. Lei, X. Lu and G. Li, *Adv. Funct. Mater.*, 2019, 1900092.
49 Y. Deng, X. Zheng, Y. Bai, Q. Wang, J. Zhao and J. Huang, *Nat. Energy*, 2018, **3**, 560–566.
50 M. A. Green, Y. Hishikawa, E. D. Dunlop, D. H. Levi, J. Hohl-Ebinger, M. Yoshita and A. W. Y. Ho-Baillie, *Prog. Photovolt. Res. Appl.*, 2019, **27**, 3–12.
51 M. He, B. Li, X. Cui, B. Jiang, Y. He, Y. Chen, D. O'Neil, P. Szymanski, M. A. EI-Sayed, J. Huang and Z. Lin, *Nat. Commun.*, 2017, **8**, 16045.
52 J. G. Tait, S. Manghooli, W. Qiu, L. Rakocevic, L. Kootstra, M. Jaysankar, C. A. Masse de la Huerta, U. W. Paetzold, R. Gehlhaar, D. Cheyns, P. Heremans and J. Poortmans, *J. Mater. Chem. A*, 2016, **4**, 3792–3797.
53 Q. Zhang, M. M. Tavakoli, L. Gu, D. Zhang, L. Tang, Y. Gao, J. Guo, Y. Lin, S.-F. Leung, S. Poddar, Y. Fu and Z. Fan, *Nat. Commun.*, 2019, **10**, 727.
54 K. Lin, J. Xing, L. N. Quan, F. P. G. de Arquer, X. Gong, J. Lu, L. Xie, W. Zhao, D. Zhang, C. Yan, W. Li, X. Liu, Y. Lu, J. Kirman, E. H. Sargent, Q. Xiong and Z. Wei, *Nature*, 2018, **562**, 245–248.
55 B. Hwang and J.-S. Lee, *Nanoscale*, 2018, **10**, 8578–8584.
56 H. Kim, J. S. Han, S. G. Kim, S. Y. Kim and H. W. Jang, *J. Mater. Chem. C*, 2019, **7**, 5226–5234.
57 M. Ahmadi, T. Wu and B. Hu, *Adv. Mater.*, 2017, **29**, 1605242.
58 H. Wang and D. H. Kim, *Chem. Soc. Rev.*, 2017, **46**, 5204–5236.
59 N. T. K. Thanh, N. Maclean and S. Mahiddine, *Chem. Rev.*, 2014, **114**, 7610–7630.
60 V. F. Puntes, D. Zanchet, C. K. Erdonmez and A. P. Alivisatos, *J. Am. Chem. Soc.*, 2002, **124**, 12874–12880.
61 S. G. Kwon and T. Hyeon, *Small*, 2011, **7**, 2685–2702.
62 D. Sept and J. A. Tuszyński, *Phys. Rev. E: Stat. Phys., Plasmas, Fluids, Relat. Interdiscip. Top.*, 1994, **50**, 4906–4910.
63 S. L. Dudarev, *Phys. Rev. B: Condens. Matter Mater. Phys.*, 2000, **62**, 9325–9337.
64 P. Srivastava, A. P. Parhi, R. Ranjan, S. Satapathi and M. Bag, *ACS Appl. Energy Mater.*, 2018, **1**, 4420–4425.
65 Y. Yu, S. Yang, L. Lei and Y. Liu, *Nanoscale*, 2017, **9**, 2569–2578.
66 D. Bi, C. Yi, J. Luo, J.-D. Décoppet, F. Zhang, S. M. Zakeeruddin, X. Li, A. Hagfeldt and M. Grätzel, *Nat. Energy*, 2016, **1**, 16142.
67 Y. Zhao, H. Tan, H. Yuan, Z. Yang, J. Z. Fan, J. Kim, O. Voznyy, X. Gong, L. N. Quan, C. S. Tan, J. Hofkens, D. Yu, Q. Zhao and E. H. Sargent, *Nat. Commun.*, 2018, **9**, 1607.
68 F. T. L. Muniz, M. A. R. Miranda, C. Morilla dos Santos and J. M. Sasaki, *Acta Crystallogr., Sect. A: Found. Adv.*, 2016, **72**, 385–390.
69 A. L. Rogach, D. V. Talapin, E. V. Shevchenko, A. Kornowski, M. Haase and H. Weller, *Adv. Funct. Mater.*, 2002, **12**, 653–664.
70 D. V. Talapin, A. L. Rogach, M. Haase and H. Weller, *J. Phys. Chem. B*, 2001, **105**, 12278–12285.
71 L. J. Nagel, L. Anthony and B. Fultz, *Philos. Mag. Lett.*, 1995, **72**, 421–427.
72 A. Pimpinelli and T. L. Einstein, *Phys. Rev. Lett.*, 2007, **99**, 226102.

73 P. Audebert, P. Daguzan, A. Dos Santos, J. C. Gauthier, J. P. Geindre, S. Guizard, G. Hamoniaux, K. Krastev, P. Martin, G. Petite and A. Antonetti, *Phys. Rev. Lett.*, 1994, **73**, 1990–1993.
74 V. K. LaMer and R. H. Dinegar, *J. Am. Chem. Soc.*, 1950, **72**, 4847–4854.
75 T. Sugimoto, *J. Colloid Interface Sci.*, 2007, **309**, 106–118.
76 Q. Hu, L. Zhao, J. Wu, K. Gao, D. Luo, Y. Jiang, Z. Zhang, C. Zhu, E. Schaible, A. Hexemer, C. Wang, Y. Liu, W. Zhang, M. Grätzel, F. Liu, T. P. Russell, R. Zhu and Q. Gong, *Nat. Commun.*, 2017, **8**, 15688.
77 P. P. von Weimarn, *Chem. Rev.*, 1925, **2**, 217–242.
78 J. W. Mullin, H.-M. Ang and H.-M. Ang, *Krist. Tech.*, 1977, **12**, 105–115.
79 D. A. Barlow, J. K. Baird and C.-H. Su, *J. Cryst. Growth*, 2004, **264**, 417–423.
80 J. K. Baird, S. C. Hill and J. C. Clunie, *J. Cryst. Growth*, 1999, **196**, 220–225.
81 D. Liu, W. Zhou, H. Tang, P. Fu and Z. Ning, *Sci. China: Chem.*, 2018, **61**, 1278–1284.
82 W. Ostwald, *Z. Phys. Chem.*, 1900, **34**, 495–503.
83 I. M. Lifshitz and V. V. Slyozov, *J. Phys. Chem. Solids*, 1961, **19**, 35–50.
84 Y. Guo, K. Shoyama, W. Sato, Y. Matsuo, K. Inoue, K. Harano, C. Liu, H. Tanaka and E. Nakamura, *J. Am. Chem. Soc.*, 2015, **137**, 15907–15914.
85 N. D. Pham, V. T. Tiong, D. Yao, W. Martens, A. Guerrero, J. Bisquert and H. Wang, *Nano Energy*, 2017, **41**, 476–487.
86 M. Yang, T. Zhang, P. Schulz, Z. Li, G. Li, D. H. Kim, N. Guo, J. J. Berry, K. Zhu and Y. Zhao, *Nat. Commun.*, 2016, **7**, 12305.
87 L. Zhi, Y. Li, X. Cao, Y. Li, X. Cui, D. Zhuang, L. Ci and J. Wei, *ACS Appl. Energy Mater.*, 2019, **2**, 320–327.
88 Z. Li, T. R. Klein, D. H. Kim, M. Yang, J. J. Berry, M. F. A. M. van Hest and K. Zhu, *Nat. Rev. Mater.*, 2018, **3**, 18017.
89 E. H. Jung, N. J. Jeon, E. Y. Park, C. S. Moon, T. J. Shin, T.-Y. Yang, J. H. Noh and J. Seo, *Nature*, 2019, **567**, 511–515.
90 W. Ke, D. Zhao, C. Xiao, C. Wang, A. J. Cimaroli, C. R. Grice, M. Yang, Z. Li, C.-S. Jiang, M. Al-Jassim, K. Zhu, M. G. Kanatzidis, G. Fang and Y. Yan, *J. Mater. Chem. A*, 2016, **4**, 14276–14283.
91 D. Yang, X. Zhou, R. Yang, Z. Yang, W. Yu, X. Wang, C. Li, S. Liu and R. P. H. Chang, *Energy Environ. Sci.*, 2016, **9**, 3071–3078.
92 K. Wojciechowski, S. D. Stranks, A. Abate, G. Sadoughi, A. Sadhanala, N. Kopidakis, G. Rumbles, C.-Z. Li, R. H. Friend, A. K.-Y. Jen and H. J. Snaith, *ACS Nano*, 2014, **8**, 12701–12709.
93 R. Chen, J. Cao, Y. Wu, X. Jing, B. Wu and N. Zheng, *Adv. Mater. Interfaces*, 2017, **4**, 1700897.
94 M. Wang, X. Jiang, J. Bian, Y. Feng, C. Wang, Y. Huang, Y. Zhang and Y. Shi, *ACS Appl. Mater. Interfaces*, 2019, **11**, 2989–2996.
95 M.-R. Ahmadian-Yazdi and M. Eslamian, *Mater. Today Commun.*, 2018, **14**, 151–159.
96 Y. Galagan, E. W. C. Coenen, W. J. H. Verhees and R. Andriessen, *J. Mater. Chem. A*, 2016, **4**, 5700–5705.
97 Y. Galagan, *J. Phys. Chem. Lett.*, 2018, **9**, 4326–4335.
98 J. Gu, J. Wu, C. Jin, X. Sun, B. Yin, G. C. Zhang, B. Wen and F. Gao, *Nanoscale*, 2018, **10**, 17722–17729.
99 F. Ye, H. Chen, F. Xie, W. Tang, M. Yin, J. He, E. Bi, Y. Wang, X. Yang and L. Han, *Energy Environ. Sci.*, 2016, **9**, 2295–2301.
100 J. Ávila, C. Momblona, P. P. Boix, M. Sessolo and H. J. Bolink, *Joule*, 2017, **1**, 431–442.
101 L. K. Ono, M. R. Leyden, S. Wang and Y. Qi, *J. Mater. Chem. A*, 2016, **4**, 6693–6713.
102 U. A. Charles, M. A. Ibrahim and M. A. M. Teridi, *J. Power Sources*, 2018, **378**, 717–731.
103 H. Chen, Z. Wei, X. Zheng and S. Yang, *Nano Energy*, 2015, **15**, 216–226.
104 T. Negami, T. Satoh, Y. Hashimoto, S. Nishiwaki, S. Shimakawa and S. Hayashi, *Sol. Energy Mater. Sol. Cells*, 2001, **67**, 1–9.
105 T. L. Chu, *Sol. Cells*, 1988, **23**, 31–48.
106 P. Brogueira, V. Chu, A. C. Ferro and J. P. Conde, *J. Vac. Sci. Technol., A*, 1997, **15**, 2968–2982.
107 X. Chen, H. Cao, H. Yu, H. Zhu, H. Zhou, L. Yang and S. Yin, *J. Mater. Chem. A*, 2016, **4**, 9124–9132.
108 M. Liu, M. B. Johnston and H. J. Snaith, *Nature*, 2013, **501**, 395–398.
109 M. K. Assadi, S. Bakhoda, R. Saidur and H. Hanaei, *Renewable Sustainable Energy Rev.*, 2018, **81**, 2812–2822.
110 Q. Chen, H. Zhou, Z. Hong, S. Luo, H.-S. Duan, H.-H. Wang, Y. Liu, G. Li and Y. Yang, *J. Am. Chem. Soc.*, 2014, **136**, 622–625.
111 M. R. Leyden, M. V. Lee, S. R. Raga and Y. Qi, *J. Mater. Chem. A*, 2015, **3**, 16097–16103.
112 P. Luo, Z. Liu, W. Xia, C. Yuan, J. Cheng and Y. Lu, *J. Mater. Chem. A*, 2015, **3**, 12443–12451.
113 T. Todorov, T. Gershon, O. Gunawan, Y. S. Lee, C. Sturdevant, L.-Y. Chang and S. Guha, *Adv. Energy Mater.*, 2015, **5**, 1500799.
114 J. Guillemoles, P. Cowache, A. Lusson, K. Fezzaa, F. Boisivon, J. Vedel and D. Lincot, *J. Appl. Phys.*, 1996, **79**, 7293–7302.
115 G. Hodes and D. Cahen, *Sol. Cells*, 1986, **16**, 245–254.
116 J. S. Blakemore, *J. Appl. Phys.*, 1982, **53**, R123–R181.
117 G. A. Ozin, *Adv. Mater.*, 1992, **4**, 612–649.
118 R. N. Bhattacharya, *Sol. Energy Mater. Sol. Cells*, 2013, **113**, 96–99.
119 F. Long, W. Wang, J. Du and Z. Zou, *J. Phys.: Conf. Ser.*, 2009, **152**, 012074.
120 D.-H. Xia and Y. Behnamian, *Russ. J. Electrochem.*, 2015, **51**, 593–601.
121 S. Ahmed, K. B. Reuter, O. Gunawan, L. Guo, L. T. Romankiw and H. Deligianni, *Adv. Energy Mater.*, 2012, **2**, 253–259.
122 G. Popov, M. Mattinen, M. L. Kemell, M. Ritala and M. Leskelä, *ACS Omega*, 2016, **1**, 1296–1306.
123 J. A. Koza, J. C. Hill, A. C. Demster and J. A. Switzer, *Chem. Mater.*, 2016, **28**, 399–405.

124 X.-P. Cui, K.-J. Jiang, J.-H. Huang, X.-Q. Zhou, M.-J. Su, S.-G. Li, Q.-Q. Zhang, L.-M. Yang and Y.-L. Song, *Chem. Commun.*, 2015, **51**, 1457–1460.
125 J. Huang, K. Jiang, X. Cui, Q. Zhang, M. Gao, M. Su, L. Yang and Y. Song, *Sci. Rep.*, 2015, **5**, 15889.
126 D. Bi, S.-J. Moon, L. Häggman, G. Boschloo, L. Yang, E. M. J. Johansson, M. K. Nazeeruddin, M. Grätzel and A. Hagfeldt, *RSC Adv.*, 2013, **3**, 18762.
127 X. Xia, W. Wu, H. Li, B. Zheng, Y. Xue, J. Xu, D. Zhang, C. Gao and X. Liu, *RSC Adv.*, 2016, **6**, 14792–14798.
128 P. S. Chandrasekhar, N. Kumar, S. K. Swami, V. Dutta and V. K. Komarala, *Nanoscale*, 2016, **8**, 6792–6800.
129 K. Hwang, Y.-S. Jung, Y.-J. Heo, F. H. Scholes, S. E. Watkins, J. Subbiah, D. J. Jones, D.-Y. Kim and D. Vak, *Adv. Mater.*, 2015, **27**, 1241–1247.
130 H.-S. Ko, J.-W. Lee and N.-G. Park, *J. Mater. Chem. A*, 2015, **3**, 8808–8815.
131 Q. Tai, P. You, H. Sang, Z. Liu, C. Hu, H. L. W. Chan and F. Yan, *Nat. Commun.*, 2016, **7**, 11105.
132 J. Burschka, N. Pellet, S.-J. Moon, R. Humphry-Baker, P. Gao, M. K. Nazeeruddin and M. Grätzel, *Nature*, 2013, **499**, 316–319.
133 W. S. Yang, J. H. Noh, N. J. Jeon, Y. C. Kim, S. Ryu, J. Seo and S. I. Seok, *Science*, 2015, **348**, 1234–1237.
134 B. Li, W. Han, B. Jiang and Z. Lin, *ACS Nano*, 2014, **8**, 2936–2942.
135 B. Li, B. Jiang, W. Han, M. He, X. Li, W. Wang, S. W. Hong, M. Byun, S. Lin and Z. Lin, *Angew. Chem., Int. Ed.*, 2017, **56**, 4554–4559.
136 J. L. Hernandez, N. Deb, R. M. W. Wolfe, C. K. Lo, S. Engmann, L. J. Richter and J. R. Reynolds, *J. Mater. Chem. A*, 2017, **5**, 20687–20695.
137 B. Park, H. G. Jeon, J. Choi, Y. K. Kim, J. Lim, J. Jung, S. Y. Cho and C. Lee, *J. Mater. Chem.*, 2012, **22**, 5641.
138 J. Y. Seok and M. Yang, *Adv. Mater. Technol.*, 2016, **1**, 1600029.
139 S. Engmann, H. W. Ro, A. A. Herzing, D. M. DeLongchamp, C. R. Snyder, L. J. Richter, A. Barito and D. J. Gundlach, *J. Mater. Chem. A*, 2017, **5**, 6893–6904.
140 K. Zhao, H. Hu, E. Spada, L. K. Jagadamma, B. Yan, M. Abdelsamie, Y. Yang, L. Yu, R. Munir, R. Li, G. O. N. Ndjawa and A. Amassian, *J. Mater. Chem. A*, 2016, **4**, 16036–16046.
141 G. Ji, W. Zhao, J. Wei, L. Yan, Y. Han, Q. Luo, S. Yang, J. Hou and C.-Q. Ma, *J. Mater. Chem. A*, 2019, **7**, 212–220.
142 S. Razza, F. Di Giacomo, F. Matteocci, L. Cinà, A. L. Palma, S. Casaluci, P. Cameron, A. D'Epifanio, S. Licoccia, A. Reale, T. M. Brown and A. Di Carlo, *J. Power Sources*, 2015, **277**, 286–291.
143 D. Khim, H. Han, K.-J. Baeg, J. Kim, S.-W. Kwak, D.-Y. Kim and Y.-Y. Noh, *Adv. Mater.*, 2013, **25**, 4302–4308.
144 C.-H. Tan, H. C. Wong, Z. Li, D. G. Bucknall, J. R. Durrant and J. T. Cabral, *J. Mater. Chem. C*, 2015, **3**, 9551–9558.
145 Y.-P. Lin, Y. Zhang and M.-F. Yu, *Adv. Mater. Technol.*, 2019, **4**, 1800393.
146 J. Wang, M. Liang, Y. Fang, T. Qiu, J. Zhang and L. Zhi, *Adv. Mater.*, 2012, **24**, 2874–2878.
147 R. Hanumanthu and L. E. Scriven, *Tappi J.*, 1996, **79**, 126–138.
148 C. E. Murphy, L. Yang, S. Ray, L. Yu, S. Knox and N. Stingelin, *J. Appl. Phys.*, 2011, **110**, 093523.
149 D. Khim, H. Han, K. J. Baeg, J. Kim, S. W. Kwak, D. Y. Kim and Y. Y. Noh, *Adv. Mater.*, 2013, **25**, 4302–4308.
150 J. Ouyang, T.-F. Guo, Y. Yang, H. Higuchi, M. Yoshioka and T. Nagatsuka, *Adv. Mater.*, 2002, **14**, 915.
151 T. Kitano, Y. Maeda and T. Akasaka, *Carbon*, 2009, **47**, 3559–3565.
152 Y. Ju, S. Y. Park, K. M. Yeom, J. H. Noh and H. S. Jung, *ACS Appl. Mater. Interfaces*, 2019, **11**, 11537–11544.
153 D.-N. Jeong, D.-K. Lee, S. Seo, S. Y. Lim, Y. Zhang, H. Shin, H. Cheong and N.-G. Park, *ACS Energy Lett.*, 2019, **4**, 1189–1195.
154 G. Cotella, J. Baker, D. Worsley, F. De Rossi, C. Pleydell-Pearce, M. Carnie and T. Watson, *Sol. Energy Mater. Sol. Cells*, 2017, **159**, 362–369.
155 C. Zuo, D. Vak, D. Angmo, L. Ding and M. Gao, *Nano Energy*, 2018, **46**, 185–192.
156 S. Das, B. Yang, G. Gu, P. C. Joshi, I. N. Ivanov, C. M. Rouleau, T. Aytug, D. B. Geohegan and K. Xiao, *ACS Photonics*, 2015, **2**, 680–686.
157 J. H. Heo, M. H. Lee, M. H. Jang and S. H. Im, *J. Mater. Chem. A*, 2016, **4**, 17636–17642.
158 Z. Liang, S. Zhang, X. Xu, N. Wang, J. Wang, X. Wang, Z. Bi, G. Xu, N. Yuan and J. Ding, *RSC Adv.*, 2015, **5**, 60562–60569.
159 S. C. Hong, G. Lee, K. Ha, J. Yoon, N. Ahn, W. Cho, M. Park and M. Choi, *ACS Appl. Mater. Interfaces*, 2017, **9**, 7879–7884.
160 F. Xu, T. Zhang, G. Li and Y. Zhao, *J. Mater. Chem. A*, 2017, **5**, 11450–11461.
161 Z. Wei, H. Chen, K. Yan and S. Yang, *Angew. Chem., Int. Ed.*, 2014, **53**, 13239–13243.
162 S.-G. Li, K.-J. Jiang, M.-J. Su, X.-P. Cui, J.-H. Huang, Q.-Q. Zhang, X.-Q. Zhou, L.-M. Yang and Y.-L. Song, *J. Mater. Chem. A*, 2015, **3**, 9092–9097.
163 F. Mathies, T. Abzieher, A. Hochstuhl, K. Glaser, A. Colsmann, U. W. Paetzold, G. Hernandez-Sosa, U. Lemmer and A. Quintilla, *J. Mater. Chem. A*, 2016, **4**, 19207–19213.
164 J. Liu, Y. Li, S. Arumugam, J. Tudor and S. Beeby, *Mater. Today: Proc.*, 2018, **5**, 13753–13758.
165 S. Ito, P. Chen, P. Comte, M. K. Nazeeruddin, P. Liska, P. Péchy and M. Grätzel, *Prog. Photovolt. Res. Appl.*, 2007, **15**, 603–612.
166 Z. Bao, J. A. Rogers and H. E. Katz, *J. Mater. Chem.*, 1999, **9**, 1895–1904.
167 A. Mei, X. Li, L. Liu, Z. Ku, T. Liu, Y. Rong, M. Xu, M. Hu, J. Chen, Y. Yang, M. Gratzel and H. Han, *Science*, 2014, **345**, 295–298.
168 Z. Ku, Y. Rong, M. Xu, T. Liu and H. Han, *Sci. Rep.*, 2013, **3**, 3132.
169 X. Li, M. Tschumi, H. Han, S. S. Babkair, R. A. Alzubaydi, A. A. Ansari, S. S. Habib, M. K. Nazeeruddin, S. M. Zakeeruddin and M. Grätzel, *Energy Technol.*, 2015, **3**, 551–555.

170 A. Priyadarshi, L. J. Haur, P. Murray, D. Fu, S. Kulkarni, G. Xing, T. C. Sum, N. Mathews and S. G. Mhaisalkar, *Energy Environ. Sci.*, 2016, **9**, 3687–3692.
171 F. Huang, Y. Dkhissi, W. Huang, M. Xiao, I. Benesperi, S. Rubanov, Y. Zhu, X. Lin, L. Jiang, Y. Zhou, A. Gray-Weale, J. Etheridge, C. R. McNeill, R. A. Caruso, U. Bach, L. Spiccia and Y.-B. Cheng, *Nano Energy*, 2014, **10**, 10–18.
172 M. Konstantakou, D. Perganti, P. Falaras and T. Stergiopoulos, *Crystals*, 2017, **7**, 291.
173 M. Xiao, L. Zhao, M. Geng, Y. Li, B. Dong, Z. Xu, L. Wan, W. Li and S. Wang, *Nanoscale*, 2018, **10**, 12141–12148.
174 B. Ding, Y. Li, S.-Y. Huang, Q.-Q. Chu, C.-X. Li, C.-J. Li and G.-J. Yang, *J. Mater. Chem. A*, 2017, **5**, 6840–6848.
175 M. Singh, A. Ng, Z. Ren, H. Hu, H.-C. Lin, C.-W. Chu and G. Li, *Nano Energy*, 2019, **60**, 275–284.
176 Y. Yu, S. Yang, L. Lei, Q. Cao, J. Shao, S. Zhang and Y. Liu, *ACS Appl. Mater. Interfaces*, 2017, **9**, 3667–3676.
177 M. Yin, F. Xie, H. Chen, X. Yang, F. Ye, E. Bi, Y. Wu, M. Cai and L. Han, *J. Mater. Chem. A*, 2016, **4**, 8548–8553.
178 G. E. Eperon, T. Leijtens, K. A. Bush, R. Prasanna, T. Green, J. T.-W. Wang, D. P. McMeekin, G. Volonakis, R. L. Milot, R. May, A. Palmstrom, D. J. Slotcavage, R. A. Belisle, J. B. Patel, E. S. Parrott, R. J. Sutton, W. Ma, F. Moghadam, B. Conings, A. Babayigit, H.-G. Boyen, S. Bent, F. Giustino, L. M. Herz, M. B. Johnston, M. D. McGehee and H. J. Snaith, *Science*, 2016, **354**, 861–865.
179 Y. Zhou, M. Yang, W. Wu, A. L. Vasiliev, K. Zhu and N. P. Padture, *J. Mater. Chem. A*, 2015, **3**, 8178–8184.
180 P. Zhao, B. J. Kim, X. Ren, D. G. Lee, G. J. Bang, J. B. Jeon, W. Bin Kim and H. S. Jung, *Adv. Mater.*, 2018, **30**, 1802763.
181 J. Ye, X. Zhang, L. Zhu, H. Zheng, G. Liu, H. Wang, T. Hayat, X. Pan and S. Dai, *Sustainable Energy Fuels*, 2017, **1**, 907–914.
182 J. Kim, J. S. Yun, Y. Cho, D. S. Lee, B. Wilkinson, A. M. Soufiani, X. Deng, J. Zheng, A. Shi, S. Lim, S. Chen, Z. Hameiri, M. Zhang, C. F. J. Lau, S. Huang, M. A. Green and A. W. Y. Ho-Baillie, *ACS Energy Lett.*, 2017, **2**, 1978–1984.
183 J. E. Bishop, T. J. Routledge and D. G. Lidzey, *J. Phys. Chem. Lett.*, 2018, **9**, 1977–1984.
184 R. Singh, I. M. Noor, P. K. Singh, B. Bhattacharya and A. K. Arof, *J. Mol. Struct.*, 2018, **1158**, 229–233.
185 Y. Galagan, F. Di Giacomo, H. Gorter, G. Kirchner, I. de Vries, R. Andriessen and P. Groen, *Adv. Energy Mater.*, 2018, **8**, 1801935.
186 Y. Zhong, R. Munir, J. Li, M.-C. Tang, M. R. Niazi, K. Zhao and A. Amassian, *ACS Energy Lett.*, 2018, **5**, 1049.
187 H. Back, J. Kim, G. Kim, T. Kyun Kim, H. Kang, J. Kong, S. Ho Lee and K. Lee, *Sol. Energy Mater. Sol. Cells*, 2016, **144**, 309–315.
188 W.-Q. Wu, Q. Wang, Y. Fang, Y. Shao, S. Tang, Y. Deng, H. Lu, Y. Liu, T. Li, Z. Yang, A. Gruverman and J. Huang, *Nat. Commun.*, 2018, **9**, 1625.
189 E. Parvazian, A. Abdollah-zadeh, H. R. Akbari and N. Taghavinia, *Sol. Energy Mater. Sol. Cells*, 2019, **191**, 148–156.
190 X. Li, D. Bi, C. Yi, J.-D. Décoppet, J. Luo, S. M. Zakeeruddin, A. Hagfeldt and M. Grätzel, *Science*, 2016, **8060**, 1–10.
191 Y. Zhao and K. Zhu, *J. Phys. Chem. C*, 2014, **118**, 9412–9418.
192 C. Zuo and L. Ding, *Nanoscale*, 2014, **6**, 9935.
193 Y. Chen, Y. Zhao and Z. Liang, *Chem. Mater.*, 2015, **27**, 1448–1451.
194 N. Yantara, F. Yanan, C. Shi, H. A. Dewi, P. P. Boix, S. G. Mhaisalkar and N. Mathews, *Chem. Mater.*, 2015, **27**, 2309–2314.
195 H. Yu, F. Wang, F. Xie, W. Li, J. Chen and N. Zhao, *Adv. Funct. Mater.*, 2014, **7**, 8735.
196 C. M. M. Soe, C. C. Stoumpos, B. Harutyunyan, E. F. Manley, L. X. Chen, M. J. Bedzyk, T. J. Marks and M. G. Kanatzidis, *ChemSusChem*, 2016, **9**, 2656–2665.
197 C. C. Stoumpos and M. G. Kanatzidis, *Acc. Chem. Res.*, 2015, **48**, 2791–2802.
198 G. Li, T. Zhang, N. Guo, F. Xu, X. Qian and Y. Zhao, *Angew. Chem., Int. Ed.*, 2016, **55**, 13460–13464.
199 P. K. Nayak, D. T. Moore, B. Wenger, S. Nayak, A. A. Haghighirad, A. Fineberg, N. K. Noel, O. G. Reid, G. Rumbles, P. Kukura, K. A. Vincent and H. J. Snaith, *Nat. Commun.*, 2016, **7**, 13303.
200 H. Zhang, J. Mao, H. He, D. Zhang, H. L. Zhu, F. Xie, K. S. Wong, M. Grätzel and W. C. H. Choy, *Adv. Energy Mater.*, 2015, **5**, 1501354–1501363.
201 P.-W. Liang, C.-Y. Liao, C.-C. Chueh, F. Zuo, S. T. Williams, X.-K. Xin, J. Lin and A. K.-Y. Jen, *Adv. Mater.*, 2014, **26**, 3748–3754.
202 J.-Y. Seo, T. Matsui, J. Luo, J.-P. Correa-Baena, F. Giordano, M. Saliba, K. Schenk, A. Ummadisingu, K. Domanski, M. Hadadian, A. Hagfeldt, S. M. Zakeeruddin, U. Steiner, M. Grätzel and A. Abate, *Adv. Energy Mater.*, 2016, **6**, 1600767–1600772.
203 W. Zhou, D. Li, Z. Xiao, Z. Wen, M. Zhang, W. Hu, X. Wu, M. Wang, W. Zhang, Y. Lu, S. Yang and S. Yang, *Adv. Funct. Mater.*, 2019, **29**, 1901026.
204 X. Liu, J. Wu, Q. Guo, Y. Yang, H. Luo, Q. Liu, X. Wang, X. He, M. Huang and Z. Lan, *J. Mater. Chem. A*, 2019, **7**, 11764–11770.
205 Y. Xia, C. Ran, Y. Chen, Q. Li, N. Jiang, C. Li, Y. Pan, T. Li, J. Wang and W. Huang, *J. Mater. Chem. A*, 2017, **5**, 3193–3202.
206 L. Chao, Y. Xia, B. Li, G. Xing, Y. Chen and W. Huang, *Chem*, 2019, **5**, 995–1006.
207 Y.-J. Jeon, S. Lee, R. Kang, J.-E. Kim, J.-S. Yeo, S.-H. Lee, S.-S. Kim, J.-M. Yun and D.-Y. Kim, *Sci. Rep.*, 2015, **4**, 6953.
208 Y. Zhang, P. Gao, E. Oveisi, Y. Lee, Q. Jeangros, G. Grancini, S. Paek, Y. Feng and M. K. Nazeeruddin, *J. Am. Chem. Soc.*, 2016, **138**, 14380–14387.
209 M. Qin, K. Tse, T. Lau, Y. Li, C. Su, G. Yang, J. Chen, J. Zhu, U. Jeng, G. Li, H. Chen and X. Lu, *Adv. Mater.*, 2019, 1901284.
210 Y. Zhong, R. Munir, J. Li, M.-C. Tang, M. R. Niazi, D.-M. Smilgies, K. Zhao and A. Amassian, *ACS Energy Lett.*, 2018, **3**, 1078–1085.
211 G. Niu, X. Guo and L. Wang, *J. Mater. Chem. A*, 2015, **3**, 8970–8980.

212 H.-S. Kim, J.-Y. Seo and N.-G. Park, *ChemSusChem*, 2016, **9**, 2528–2540.
213 J. E. Lee, S. Bae, W. Oh, H. Park, S. M. Kim, D. Lee, J. Nam, C. Bin Mo, D. Kim, J. Yang, Y. Kang, H. Lee and D. Kim, *Prog. Photovolt. Res. Appl.*, 2016, **24**, 1035–1043.
214 H. Hu, W. Deng, M. Qin, H. Yin, T.-K. Lau, P. W. K. Fong, Z. Ren, Q. Liang, L. Cui, H. Wu, X. Lu, W. Zhang, I. McCulloch and G. Li, *Materials Today Energy*, 2019, **12**, 398–407.
215 L. Wang, H. Zhou, J. Hu, B. Huang, M. Sun, B. Dong, G. Zheng, Y. Huang, Y. Chen, L. Li, Z. Xu, N. Li, Z. Liu, Q. Chen, L.-D. Sun and C.-H. Yan, *Science*, 2019, **363**, 265–270.
216 S. Yang, S. Chen, E. Mosconi, Y. Fang, X. Xiao, C. Wang, Y. Zhou, Z. Yu, J. Zhao, Y. Gao, F. De Angelis and J. Huang, *Science*, 2019, **365**, 473–478.
217 I. C. Smith, E. T. Hoke, D. Solis-Ibarra, M. D. McGehee and H. I. Karunadasa, *Angew. Chem., Int. Ed.*, 2014, **53**, 11232–11235.
218 T. M. Koh, V. Shanmugam, J. Schlipf, L. Oesinghaus, P. Müller-Buschbaum, N. Ramakrishnan, V. Swamy, N. Mathews, P. P. Boix and S. G. Mhaisalkar, *Adv. Mater.*, 2016, **28**, 3653–3661.
219 N. Li, Z. Zhu, C.-C. Chueh, H. Liu, B. Peng, A. Petrone, X. Li, L. Wang and A. K.-Y. Jen, *Adv. Energy Mater.*, 2017, **7**, 1601307.
220 Z. Wang, Q. Lin, F. P. Chmiel, N. Sakai, L. M. Herz and H. J. Snaith, *Nat. Energy*, 2017, **2**, 17135.
221 G. Grancini, C. Roldán-Carmona, I. Zimmermann, E. Mosconi, X. Lee, D. Martineau, S. Narbey, F. Oswald, F. De Angelis, M. Graetzel and M. K. Nazeeruddin, *Nat. Commun.*, 2017, **8**, 15684.
222 P. Wang, X. Zhang, Y. Zhou, Q. Jiang, Q. Ye, Z. Chu, X. Li, X. Yang, Z. Yin and J. You, *Nat. Commun.*, 2018, **9**, 2225.
223 Y. Wang, M. I. Dar, L. K. Ono, T. Zhang, M. Kan, Y. Li, L. Zhang, X. Wang, Y. Yang, X. Gao, Y. Qi, M. Grätzel and Y. Zhao, *Science*, 2019, **365**, 591–595.
224 X. Zhang, X. Ren, B. Liu, R. Munir, X. Zhu, D. Yang, J. Li, Y. Liu, D.-M. Smilgies, R. Li, Z. Yang, T. Niu, X. Wang, A. Amassian, K. Zhao and S. Liu, *Energy Environ. Sci.*, 2017, **10**, 2095–2102.
225 P. Cheng, Z. Xu, J. Li, Y. Liu, Y. Fan, L. Yu, D.-M. Smilgies, C. Müller, K. Zhao and S. F. Liu, *ACS Energy Lett.*, 2018, **3**, 1975–1982.

